An Improved Model-Free Predictive Current Control of PMSM Drives Based on a Novel Finite-Time Extended State Observer

Changliang Dang, Yuanlin Wang, *Member, IEEE*, Jinli Lei, and Wenjuan Zhang

***Abstract*—Due to the independence of motor parameters, the ultralocal model-based model-free predictive current control strategy (MFPCC) for permanent magnet synchronous motors (PMSMs) fundamentally addresses the model mismatch problem caused by parameter perturbations, making it particularly suitable for complex electrical applications, such as electric vehicles, robotic drives, and aerospace actuators. The conventional MFPCC utilizes a linear extended state observer (LESO), which achieves only asymptotic convergence of observation errors. In addition, LESO is not adequately equipped to handle periodic disturbances caused by current harmonics due to nonlinear factors. Therefore, this article proposes a novel finite-time extended state observer (NFTESO) that combines the complex coefficient filter with an observation error-based bandwidth tuning scheme to enhance estimation accuracy and improve current harmonic suppression performance. Meanwhile, the finite-time Lyapunov stability of the NFTESO is theoretically analyzed. With both aperiodic and periodic disturbances observed and compensated, the steady-state and transient performance of the proposed NFTESO-MFPCC is significantly enhanced. Furthermore, the closed-loop stability of the control system is discussed, and the parameter tuning strategy is provided. Comprehensive experiments on a 1.6-kW PMSM test bench verify that the proposed NFTESO-MFPCC control scheme can simultaneously mitigate both aperiodic and periodic disturbances in the current loop while preserving the advantages of MFPCC.**

***Index Terms*—Harmonics suppression, model-free predictive current control (MFPCC), parameter mismatch, ultralocal model.**

I. Introduction

PERMANENT magnet synchronous motors (PMSMs) have been widely used in fields, such as electric vehicles [1], more electrical aircraft [2], railway traction systems [3], and electric ships [4], due to their advantages of simple structure, high reliability, high power density, and high torque current ratio. It can be foreseen that PMSM will play an increasingly important role in the application scenarios of transportation electrification. At present, various nonlinear control strategies have been developed to improve the performance, including fuzzy control [5], adaptive control [6], active disturbance rejection control (ADRC) [7], sliding-mode control [8], model predictive control (MPC) [9], [10], and so on. Among them, MPC utilizes a mathematical model to discretize the predicted value at the next moment and follow that value along the reference trajectory, which is a hotpot due to its intuitive concept and excellent dynamic performance [11]. However, the control performance depends on the precise mathematical model of PMSM. Unfortunately, in practical applications, parameter mismatch is inevitable. For instance, the inductance value is easily influenced by magnetic flux density perturbation, while the resistance value is affected by temperature. To solve the issue, there are three common categories of solutions, including the observer method [12], the parameter identification method [13], and the model-free method [14], [15], [16].

The first two methods can estimate parameter perturbation to a certain extent; however, the initial nominal parameters of the PMSM are still required. To solve this problem fundamentally, model-free predictive current control (MFPCC) has obtained widespread attention and is being developed. An enhanced extended state observer (ESO) was proposed in [14] to identify the motor inductance and achieve model-free control. A current prediction model was constructed in [15], which only included current and voltage errors. In [16], a model-free control method based on system input and output information was proposed, avoiding the influence of parameter mismatch and the problem of update stagnation.

However, the aperiodic disturbance includes motor parameter perturbations, unmodeled dynamics, and other external uncertainties. The other is the periodic disturbance, including magnetic flux and voltage harmonics introduced by the inverter nonlinearity [17]. The linear extended state observer (LESO) is often employed in MFPCC to observe the stator current and the lumped uncertainty. The LESO-MFPCC can eliminate the effect of aperiodic perturbations, but LESO has a poor ability to suppress time-varying disturbances. Although increasing the

Received 21 June 2025; revised 27 September 2025 and 29 November 2025; accepted 19 December 2025. Date of publication 30 December 2025; date of current version 20 March 2026. This work was supported in part by the Shaanxi Provincial Central Guidance Local Science and Technology Development Project under Grant 2024ZY-JCYJ-01-07 and in part by the Key Research and Development Projects of Shaanxi Province under Grant 2022GXLH-02-06. Recommended for publication by Associate Editor C. Rojas. *(Corresponding author: Yuanlin Wang.)*

Changliang Dang is with the Baoji University of Arts and Sciences, Baoji 721016, China, and also with Northwestern Polytechnical University, Xi'an 710072, China (e-mail: dcl312@mail.nwpu.edu.cn).

Yuanlin Wang is with Northwestern Polytechnical University, Xi'an 710072, China (e-mail: yuanlin.wang@nwpu.edu.cn).

Jinli Lei and Wenjuan Zhang are with the Baoji University of Arts and Sciences, Baoji 721016, China (e-mail: kitty@mail.nwpu.edu.cn; zhangwenjuan@bjwlxy.edu.cn).

Color versions of one or more figures in this article are available at https://doi.org/10.1109/TPEL.2025.3649261.

Digital Object Identifier 10.1109/TPEL.2025.3649261

bandwidth can improve the anti-interference ability, it also introduces high-frequency noise, which deteriorates the performance. More importantly, the estimation error of LESO can only ensure asymptotic convergence to the origin, and the robustness to parameter mismatch is not ideal [18]. A high-gain ESO was constructed to improve compensation accuracy and dynamic performance in [19]. In [20], an LESO was designed in the current loop of DPCC. In [21], an enhanced ESO-based MFPCC method was developed to eliminate the effects of high-frequency (HF) perturbation.

Furthermore, regarding periodic disturbances, introducing auxiliary components is currently the mainstream direction of research. In [22], a generalized integrator-extended state observer (GIESO) was proposed to observe the fast sinusoidal disturbances in grid-connected converters. In [23], an adaptive GIESO was developed to realize a smooth speed control performance. However, the antidisturbance will be attenuated when the harmonic frequency shifts. In [7], a composite controller combining quasi-resonant and ADRC was proposed to reduce the fluctuation. In [24], a quasi-resonant ESO-based predictive current control method was proposed for a three-phase rectifier. In [25], an improved GIESO was developed to promote the accuracy of the observation of back electromotive force for the sensorless control of PMSM drives. In [26], a decoupling controller based on an adaptive quasi-resonant ESO is proposed for observing and compensating for periodic and aperiodic disturbances of the matrix torque component machine.

Furthermore, the complex coefficient filter (CCF), which can extract orthogonal signals with selective frequency and selective phase sequence, is an effective method to improve the harmonics suppression performance. In [27], the CCF was incorporated into the ESO to promote the observation accuracy of harmonic components. In [28], an adaptive CCF was developed to replace the LPF to extract the fundamental part in the applications of PMSM sensorless drives. In [29], a multiple CCF was utilized to extract positive and negative sequence components of the sixth harmonic current to eliminate the influence caused by dead time. In [30], a CCF-based improved ADRC with a disturbance-separation cascaded ESO was developed to estimate positive and negative sequence disturbances arising from converter nonlinearity for LC-filtered current source rectifiers.

This article proposes an improved MFPCC for PMSM drives to improve harmonic suppression capability, steady and transient performance, and robustness to parameter variations. The main contributions are listed as follows.

1) A novel finite-time extended state observer (NFTESO) is introduced in MFPCC for PMSM drives to suppress the aperiodic and periodic disturbances simultaneously. In addition, finite-time stability is theoretically analyzed based on Lyapunov theory.
2) Compared with the GIESO proposed in [22], the proposed NFTESO obtains a stronger suppression ability for specific harmonics and better dynamic performance.
3) Compared with the LESO-MFPCC proposed in [16], the periodic disturbance caused by inverter nonlinearity is effectively reduced.
4) The proposed control scheme retains the advantages of conventional MFPCC regarding dynamic performance, and the computation time is less than half of the sampling period in the experiment.

Table I shows the performance indices among the comparative observers, and the rest of this article is organized as follows: Section II presents the system model and analyzes the disturbance. The NFTESO-MFPCC is proposed and discussed in Section III. The comparative experimental results are presented in Section IV. Finally, Section V concludes this article.

II. Problem Formulation

A. Mathematical Model of PMSM

The research object of this article is the surface-mounted PMSM, which satisfies $L_s = L_d = L_q$. Then, the mathematical model in dq synchronous rotating coordinate can be described as

$$\begin{cases} \frac{di_d}{dt} = \frac{u_d}{L_s} - \frac{R_s}{L_s} i_d + \omega_e i_q \\ \frac{di_q}{dt} = \frac{u_q}{L_s} - \omega_e i_d - \frac{R_s i_q}{L_s} - \frac{\psi_f}{L_s}\omega_e \end{cases} \tag{1}$$

where u_d and u_q are dq-axis voltages, respectively; R_s, L_s, and ψ_f represent the resistance, inductance, and flux linkage, respectively; ω_e denotes the electrical angular velocity.

B. Disturbance Analysis

1) Aperiodic disturbance: The parameter mismatches and unmodeled dynamics will lead to aperiodic disturbances [28], which can be described as

$$\begin{cases} f_{d\_ap} = \frac{1}{L_{s0}} \left(-\Delta R_s i_d - \Delta L_s \left(\frac{di_d}{dt} + \omega_e i_q \right) \right) + \upsilon_d \\ f_{q\_ap} = \frac{1}{L_{s0}} \left(-\Delta R_s i_q - \Delta L_s \left(\frac{di_q}{dt} + \omega_e i_d \right) - \Delta \psi_f \omega_e \right) + \upsilon_q \end{cases} \tag{2}$$

where υ_d and υ_q represent the disturbance, including inverter nonlinearity and unmodeled dynamics. The parameters with $'\Delta'$ denote the variation values between the nominal values and actual values, satisfying $\Delta R_s = R_{s0} - R_s$, $\Delta L_s = L_{s0} - L_s$, and $\Delta \psi_f = \psi_{f0} - \psi_f$, with subscript $'0'$ the nominal values of PMSM parameters.

For PMSM current control systems, aperiodic disturbances include parameter variations—such as changes in resistance and flux linkage due to temperature rise—as well as inductance variations that occur when the stator current enters the saturation region. These disturbances also encompass complex high-order dynamics that are often neglected during the modeling process. A key characteristic of aperiodic disturbances is that their occurrence cannot be accurately predicted, and they do not follow a fixed periodic pattern. As a result, they cannot be effectively suppressed using frequency-specific filters (e.g., notch filters), unlike periodic disturbances such as cogging torque. In deadbeat-based current control systems, voltage errors caused by parameter deviations lead to fluctuations in the q-axis current, which in turn cause torque ripple. If these errors continue to accumulate, they can further degrade system performance, resulting in increased acoustic noise, reduced efficiency, and even a degradation in stability. Therefore, the analysis and

TABLE I
COMPARISON OF KALMAN FILTER, LESO, GIESO, AND NFTESO

Criterion	Kalman Filter	LESO	GIESO	NFTESO
Convergence	Slow; asymptotic	Slow; asymptotic	Slow; asymptotic	Fast; finite time
Estimation Accuracy	High; sensitive to model parameters mismatch and unmodeled dynamics	Medium; poor estimation accuracy of time-varying disturbances	High at target harmonic frequencies; limited to finite points	High; accurate harmonic tracking with finite-time enhancement
Harmonic Suppression	Medium; degrades if harmonics are excluded from the model	Poor; acts as a low-pass filter suppressing high-frequency components	Good; error-free estimation and compensation of specific frequency harmonic components	Excellent; suitable for harmonics with multi-frequency optimization
Robustness	Poor; relying heavily on the model accuracy and the intensity of disturbances	Medium; bandwidth-based design, sensitive to parameter changes	Medium; better than LESO, but performance degrades with frequency drift	Strong; inherits FTESO robustness and harmonic interference rejection
Anti-noise Performance	Excellent; Kalman gain provides strong noise suppression	Good; small bandwidth suppresses noise but degrades dynamic response	Medium; sensitive to measurement noise, requiring trade-off	Medium; finite-time convergence may amplify noise, requiring trade-off
Stability Analysis	Complex; based on stochastic theory and Riccati equations	Simple; linear system pole assignment, simple and mature	Medium; via frequency domain analysis of linear systems (Nyquist, Bode)	Complex; finite-time proof via Lyapunov or homogeneity theory
Computational Complexity	Highest; recursive covariance calculation	Low; linear operations, highly efficient	Medium; a linear operation with multiple resonators	High; multi-gain design and finite-time proof

suppression of aperiodic disturbances are of great significance for achieving high precision, fast dynamic response, and strong robustness.

2) Periodic disturbance: The periodic disturbance is caused by inverter nonlinearity and flux harmonics [29]. According to [31], the voltage harmonics u_h and flux harmonics ψ_{fh} can be described as

$$\begin{cases} u_{hd} = \sum_{i=1}^{\infty} u_{hdi} \sin(6i\omega_e t) \\ u_{hq} = \sum_{i=1}^{\infty} u_{hqi} \cos(6i\omega_e t) \end{cases} \tag{3}$$

$$\begin{cases} \psi_{fhd} = \sum_{i=1}^{\infty} \psi_{fhdi} \cos(6i\omega_e t) \\ \psi_{fhq} = \sum_{i=1}^{\infty} \psi_{fhqi} \sin(6i\omega_e t) \end{cases} \tag{4}$$

where u_{hd}, u_{hq}, ψ_{fhd}, and ψ_{fhq} are the amplitudes of the $6i$th-order harmonics.

Thus, the periodic disturbances can be summarized as

$$\begin{cases} f_{d\_p} = u_{hd} + \omega_e \psi_{fhd} \\ f_{q\_p} = u_{hq} + \omega_e \psi_{fhq}. \end{cases} \tag{5}$$

Accordingly, when the aperiodic and periodic disturbances are taken into account, the mathematical model of PMSM can be rewritten as

$$\begin{cases} \frac{di_d}{dt} = \frac{u_d}{L_{s0}} - \frac{R_{s0}}{L_{s0}} i_d + \omega_e i_q + f_{d\_ap} + f_{d\_p} \\ \frac{di_q}{dt} = \frac{u_q}{L_{s0}} - \frac{R_{s0}}{L_{s0}} i_q - \omega_e i_d - \frac{\psi_{f0}}{L_{s0}} \omega_e + f_{q\_ap} + f_{q\_p}. \end{cases} \tag{6}$$

It can be seen from (6) that aperiodic disturbances will inevitably cause the deviation between the command and the actual current, and the inductance perturbation will increase the current harmonic content in the PMSM drives [32]. Moreover, according to [31], periodic disturbances can produce fifth and seventh current harmonics in the stationary coordinate, both of which are converted to sixth harmonics in the dq rotating frame.

Now, most existing MFPCC and its optimization algorithms can eliminate the influence of aperiodic disturbances, while the periodic disturbances are neglected. In fact, in some high-precision equipment applications, current harmonics caused by periodic disturbances are also unbearable. Therefore, this article focuses on improving MFPCC by simultaneously eliminating the effects of both aperiodic and periodic disturbances.

C. Conventional LESO-MFPCC

According to [33], by using only the input and output signals of the system, the first-order ultralocal model of a single-input single-output system can be described as

$$\dot{y} = \varepsilon u + F \tag{7}$$

where u and y are the system input and output, respectively; F denotes the total uncertainty, and ε is a scaling factor determined by the designer.

Then, by comparing (7) with (6), the ultralocal model of PMSM can be described as

$$\begin{cases} \frac{di_d}{dt} = \varepsilon_s u_d + F_d \\ \frac{di_q}{dt} = \varepsilon_s u_q + F_q \end{cases} \tag{8}$$

where ε_s is the gain of the voltage vector. F_d and F_q can be regarded as the lumped uncertainties.

Obviously, (8) does not contain motor parameters, leading to strong robustness. However, F_d and F_q contain unknown parts, such as parameter perturbation and unmodeled dynamics, which are difficult to measure directly. Then, taking the model of q-axis as an example, a typical LESO is given as

$$\begin{cases} e_{1q} = i_q - \hat{i}_q \\ \dot{\hat{i}}_q = \varepsilon_s u_q + \hat{F}_q + \beta_1 e_{1q} \\ \dot{\hat{F}}_q = \beta_2 e_{1q} \end{cases} \tag{9}$$

where parameters with "^" denote the observed states; β_1 and β_2 represent the observer gains.

Then, by using the first-order Euler method and combining (8) and (9), the command voltage vector can be obtained as

$$\begin{cases} u_d^*(k) = \frac{i_d^* - \hat{i}_{dl}(k+1)}{\varepsilon_s T_s} - \frac{\hat{F}_{dl}(k+1)}{\varepsilon_s} \\ u_q^*(k) = \frac{i_q^* - \hat{i}_{ql}(k+1)}{\varepsilon_s T_s} - \frac{\hat{F}_{ql}(k+1)}{\varepsilon_s} \end{cases} \tag{10}$$

where T_s is the sampling period. It should be noted that to avoid confusion with the observed values of NFTESO in the following text, $\hat{i}_{dl}$ and $\hat{i}_{ql}$ denote the observed current of LESO. Similarly, $\hat{F}_{dl}$ and $\hat{F}_{ql}$ denote the observed uncertainties of LESO.

D. Limitations of LESO

By assuming the derivative of the q-axis total uncertainty satisfies $\dot{F}_q = G_q$, the error dynamics of LESO can be described as

$$\begin{cases} \dot{e}_{1q} = e_{2q} - \beta_1 e_{1q} \\ \dot{e}_{2q} = G_q - \beta_2 e_{1q}. \end{cases} \tag{11}$$

Then, (11) can be written in the form of a matrix as

$$\dot{\boldsymbol{e}}_q = A\boldsymbol{e}_q + BG_q \tag{12}$$

where $\boldsymbol{e}_q = [e_{1q} \quad e_{2q}]^\top$, $A = \begin{bmatrix} -\beta_1 & 1 \\ -\beta_2 & 0 \end{bmatrix}$, $B = [0 \quad 1]^\top$.

When $G_q = 0$ is satisfied, that is, if the disturbance is constant or changes slowly, the error dynamics can be simplified to $\dot{\boldsymbol{e}}_q = A\boldsymbol{e}_q$. The characteristic equation is expressed as

$$s^2 + \beta_1 s + \beta_2 = 0. \tag{13}$$

Therefore, it can be concluded that the error dynamics of LESO are exponentially stable. In addition, when $G_q \neq 0$, the error will converge to 0 asymptotically.

In addition, according to the bandwidth selection strategy in [17], β_1 and β_2 can be designed as

$$\beta_i = \frac{2!}{i!\,(2-i)!}\omega_0^i, \quad i = 1, 2 \tag{14}$$

where ω_0 is the bandwidth of LESO. Thus, β_1 and β_2 satisfies

$$\beta_1 = 2\omega_0, \quad \beta_2 = \omega_0^2. \tag{15}$$

Then, based on (9), the transfer function between $\hat{F}_q$ and F_q can be expressed as

$$G_{Fq}(s) = \frac{\hat{F}_q(s)}{F_q(s)} = \frac{\omega_0^2}{(s+\omega_0)^2}. \tag{16}$$

Moreover, the transfer function of the estimation error can be expressed as

$$G_{eFq}(s) = \frac{F_q(s) - \hat{F}_q(s)}{F_q(s)} = \frac{s(s+2\omega_0)}{(s+\omega_0)^2}. \tag{17}$$

It can be seen from (16) that LESO is a second-order low-pass system, and the input signal will attenuate in the high-frequency region. For the aperiodic disturbance, when β_1 and β_2 are reasonably selected, an accurate and effective estimation can be achieved. However, if the disturbance contains rapidly changing components, such as slope signals or periodic perturbations, the performance estimation will deteriorate. In addition, when the disturbance is a step signal, LESO can accurately estimate the information of the disturbance signal in the steady state. However, when the disturbance is a ramp signal with a slope of k, that is, $f(t) = kt$ ($F(s) = k/s^2$), according to the final value theorem, the LESO disturbance estimation error for the slope signal is expressed as

$$\lim_{s\to 0} G_{eFq}(s)F(s) = \lim_{s\to 0} \frac{k(s+2\omega_0)}{s^2 + 2\omega_0 s + \omega_0^2} = \frac{2k}{\omega_0}. \tag{18}$$

Therefore, from (18), it can be seen that when the disturbance is a ramp signal with a slope of k, the steady-state error exists. Although increasing the bandwidth of LESO can enhance the perturbation estimation ability, the observed values are more sensitive to noise, which should be avoided.

Moreover, to observe rapidly changing sinusoidal disturbances with relatively low bandwidth, a GIESO was proposed in [22], which is developed based on the traditional LESO, incorporating multiple resonant controllers with different resonant frequencies into the disturbance estimation loop. The resonant component can enhance the estimation of high-frequency disturbances at specific frequencies, and the transfer function of GIESO can be expressed as

$$R(s) = \frac{k_r s}{s^2 + \omega_r^2} \tag{19}$$

where k_r and ω_r denote the resonant gain and selective resonant frequency, respectively.

From (19), it is evident that GIESO can track rapidly changing sinusoidal disturbances with relatively low bandwidth. Still, it performs well only at the resonance frequency ω_r [34], [35]. In practical PMSM applications, errors arise from the discretization of sampling and control systems, as well as the fact that rotor speed may not stay completely constant, causing the obtained frequency to deviate from its true value and leading to a decline in the observing performance of GIESO.

III. Novel Finite-Time Extended State Observer-MFPCC

A. Complex Coefficient Filter

An ideal first-order CCF achieves zero phase shift and unit gain at the selected frequency, while the signals of other frequencies can be attenuated simultaneously. Accordingly, the frequency selection characteristic of CCF makes it particularly suitable for extracting specific order harmonic signals from the original signal.

A CCF in the s-domain can be described as [36]

$$G_{\mathrm{CCF}}(s) = \frac{\omega_c}{s - j\omega_r + \omega_c} \tag{20}$$

where ω_c, ω_r, and j are the cutoff frequency, selected angular frequency, and the sign of the complex number, respectively.

According to [27], the frequency-selective characteristics of CCF make it particularly suitable for extracting specific order

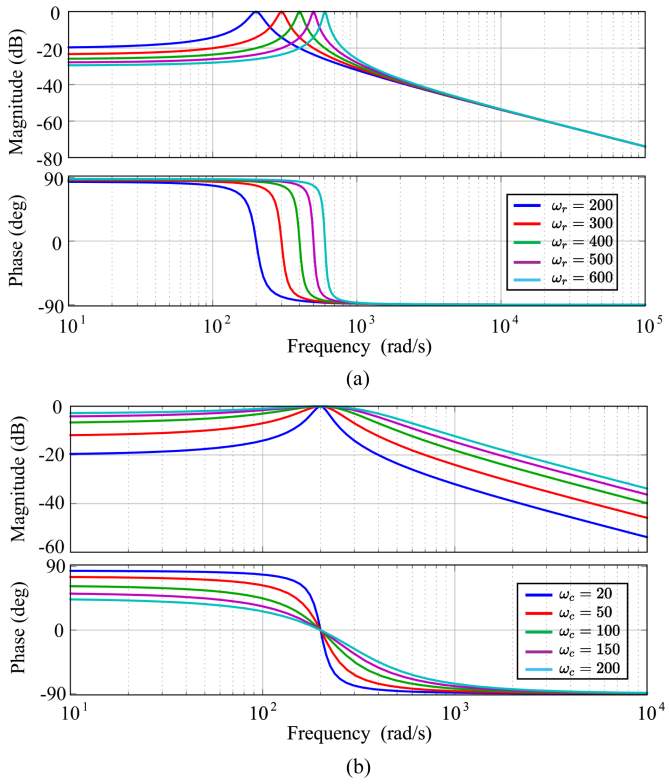

Fig. 1. Bode diagram of CCF with different parameters. (a) ω_r variation. (b) ω_c variation.

harmonic signals from the original signal. When the input signal's fundamental frequency remains constant, CCF's frequency selection performance depends on its cutoff frequency ω_c. However, when the fundamental frequency of the original signal changes, the harmonic frequency will also change accordingly. Thus, to achieve a consistent frequency response at the same order harmonic with different fundamental frequencies, the cutoff frequency of CCF is designed as

$$\omega_c = \eta|\omega_r| \tag{21}$$

where η is defined as the cutoff frequency coefficient.

Thus, the frequency response can be described as

$$\begin{cases} G_{\mathrm{CCF}}(j\omega) = \dfrac{\eta}{\sqrt{(\omega/\omega_r - 1)^2 + \eta^2}} \\ \angle G_{\mathrm{CCF}}(j\omega) = \arctan\left(\dfrac{1-\omega/\omega_r}{\eta}\right). \end{cases} \tag{22}$$

It can be seen from (22) that when η is constant, the frequency response performance of CCF depends on the ω/ω_r. The Bode diagram of CCF is shown in Fig. 1. As can be seen in Fig. 1(a), the designed resonant frequency ω_r can be extracted by CCF with unit gain and zero phase shift. Moreover, it can be concluded from Fig. 1(b) that a good harmonic attenuation performance can be achieved with a small ω_c; however, the dynamic performance demands a large ω_c. Thus, CCF needs to coordinate the relationship between harmonic attenuation performance and dynamic response.

Then, the CCF-based LESO in the d-axis can be designed as

$$\begin{cases} e_{1d} = i_d - \hat{i}_d \\ \dot{\hat{i}}_d = \varepsilon_s u_d + \hat{F}_d + \beta_1 e_{1d} \\ \dot{\hat{F}}_d = \beta_2 \left(1 + G_{\mathrm{CCF}}(t)\right) e_{1d} \end{cases} \tag{23}$$

where $G_{\mathrm{CCF}}(t)$ is the time domain expression of $G_{\mathrm{CCF}}(s)$.

The transfer function between $\hat{F}_d$ and F_d can be derived as

$$G_{Fd}(s) = \frac{\hat{F}_d(s)}{F_d(s)} = \frac{(\beta_2\omega_c + \beta_2)s + \beta_2\omega_c - j\beta_2\omega_r}{\Delta(s)} \tag{24}$$

where $\Delta(s)$ satisfies

$$\Delta(s) = s^3 + (\beta_1 + \omega_c - j\omega_r)s^2 + (\beta_1 + (\beta_1 + \beta_2)\omega_c - j\beta_1\omega_r)\, s + \beta_2\omega_c - j\beta_2\omega_r. \tag{25}$$

Thus, the transfer function of the estimation error $G_{eFd}(s)$ can be described as

$$G_{eFd}(s) = \frac{F_d(s) - \hat{F}_d(s)}{F_d(s)} = \frac{\Omega(s)}{\Delta(s)} \tag{26}$$

where $\Omega(s)$ satisfies

$$\Omega(s) = s^3 + (\beta_1 + \omega_c - j\omega_r)s^2 - (j\beta_1\omega_r - \beta_1\omega_c)s. \tag{27}$$

The frequency response of $G_{eFd}(s)$ under different parameter combinations is shown in Fig. 2. As illustrated in Fig. 2(a), when ω_r is changing with $\omega_0 = 400$ and $\eta = 0.02$, a significant amplitude attenuation exists at the resonant frequency ω_r, and zero phase shift is obtained, indicating that the harmonic disturbance with a frequency of ω_r can be accurately estimated by CCF. Meanwhile, CCF shows similar behavior to LESO in both the low and high-frequency regions.

Furthermore, the Bode plots with ω_c and ω_0 changing are shown in Fig. 2(b) and (c), respectively. Note that as ω_c decreases, the bandwidth of CCF at the resonant frequency becomes narrower, and the frequency selection ability increases; however, the peak gain remains stable. In addition, as ω_0 decreases, the amplitude-frequency curve gradually shifts upward, indicating an increase in the estimation error of CCF for harmonics. Moreover, the stability of CCF has been analyzed in [27] and [40], which is omitted here.

From the above analysis, it can be concluded that the cutoff frequency ω_c is a key parameter that determines the selection range of the filter and its ability to process signals of different frequencies. In addition, it is closely related to dynamic response: the smaller the frequency, the narrower the bandwidth of CCF, and the closer its filtering characteristic is to idealization. However, the dynamic response will decrease. On the contrary, the larger the CCF, the wider the bandwidth, and the worse the filtering characteristics, but the dynamic response can be improved. However, it should be noted that excessively high cutoff frequency can make the filter extremely sensitive to measurement noise, which may introduce noise and lead to deterioration of control performance. Therefore, the tuning of

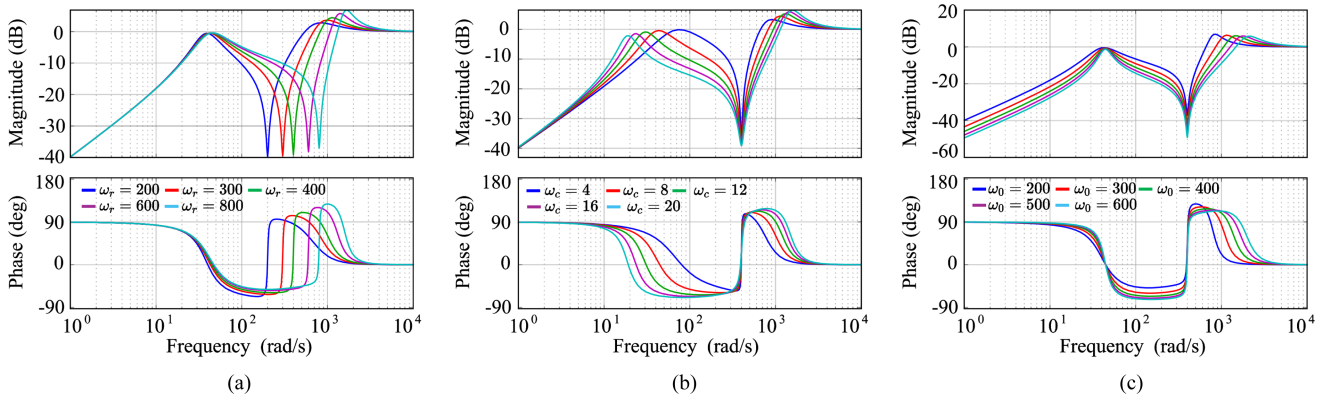

Fig. 2. Bode diagram of $G_{eFd}(s)$ with different parameters. (a) ω_r variation. (b) ω_c variation. (c) ω_0 variation.

ω_c needs to achieve an optimal balance between disturbance suppression and noise immunity.

From the above analysis, it can be seen that an excessively high cutoff frequency ω_c may not effectively filter out high-frequency noise. This type of noise will mix into the current signal, causing an increase in current ripple and deterioration of the current waveform. However, dynamic response will deteriorate with a low cutoff frequency, resulting in delayed response to load changes and fluctuations in current command signals. In this article, the cutoff frequency ω_c is obtained through theoretical analysis and multiple experiments.

B. Proposed NFTESO

Motivated by [37], the conventional FTESO for MFPCC can be constructed as

$$\begin{cases} \boldsymbol{e}_1 = \boldsymbol{i}_{dq} - \hat{\boldsymbol{i}}_{dq} \\ \dot{\hat{\boldsymbol{i}}}_{dq} = \varepsilon_s \boldsymbol{u}_{dq} + \hat{\boldsymbol{F}}_{dq} + \beta_{01}|\boldsymbol{e}_1|^{\alpha_1}\mathrm{sgn}(\boldsymbol{e}_1) \\ \dot{\hat{\boldsymbol{F}}}_1 = \beta_{02}|\boldsymbol{e}_1|^{\alpha_2}\mathrm{sgn}(\boldsymbol{e}_1) \end{cases} \tag{28}$$

where β_{01} and β_{02} are the positive gains; the coefficient $\alpha_i \in (0,1), i = 1,2$ satisfy the recurrent relations $\alpha_i = i\alpha - (i-1)$ and $\alpha_1 = \alpha$, where α belongs to an interval $(1-\varepsilon, 1)$, with ε a sufficiently small number.

Then, the error dynamics can be obtained as

$$\begin{cases} \boldsymbol{e}_2 = \boldsymbol{F}_{dq} - \hat{\boldsymbol{F}}_{dq} \\ \dot{\boldsymbol{e}}_1 = \boldsymbol{e}_2 - \beta_{01}|\boldsymbol{e}_1|^{\alpha_1}\mathrm{sgn}(\boldsymbol{e}_1) \\ \dot{\boldsymbol{e}}_2 = \boldsymbol{R}_{dq} - \beta_{02}|\boldsymbol{e}_1|^{\alpha_2}\mathrm{sgn}(\boldsymbol{e}_1) \end{cases} \tag{29}$$

where $\boldsymbol{R}_{dq}$ represents the derivatives of $\boldsymbol{F}_{dq}$.

It is worth noting that, compared with traditional LESO, the fractional power terms are introduced in the FTESO. When the estimation error converges close to the origin, the nonlinear term in (29) can ensure that the estimation error converges from the neighborhood of the origin to 0 within a finite time, which is the most significant feature of FTESO that is different from traditional LESO. However, the traditional FTESO also lacks the capability of dealing with the periodic disturbances.

By introducing CCF into FTESO, (28) can be rewritten as

$$\begin{cases} \boldsymbol{e}_1 = \boldsymbol{i}_{dq} - \hat{\boldsymbol{i}}_{dq} \\ \dot{\hat{\boldsymbol{i}}}_{dq} = \varepsilon_s \boldsymbol{u}_{dq} + \hat{\boldsymbol{F}}_{dq} + \beta_{01}|\boldsymbol{e}_{dq}|^{\alpha_1}\mathrm{sgn}(\boldsymbol{e}_1) \\ \dot{\hat{\boldsymbol{F}}}_{dq} = \beta_{02}\left(|\boldsymbol{e}_1|^{\alpha_2}\mathrm{sgn}(\boldsymbol{e}_1) + G_{\mathrm{CCF}}(\boldsymbol{e}_1)\right). \end{cases} \tag{30}$$

Then, the error dynamics can be obtained as

$$\begin{cases} \dot{\boldsymbol{e}}_1 = \boldsymbol{e}_2 - \beta_{01}|\boldsymbol{e}_1|^{\alpha_1}\mathrm{sgn}(\boldsymbol{e}_1) \\ \dot{\boldsymbol{e}}_2 = \boldsymbol{R}_{dq} - \beta_{02}|\boldsymbol{e}_1|^{\alpha_2}\mathrm{sgn}(\boldsymbol{e}_1) - \beta_{02}G_{\mathrm{CCF}}(\boldsymbol{e}_1). \end{cases} \tag{31}$$

Since it has been proved that the observation error of CCF is bounded, by defining $\boldsymbol{G}_{dq} = \boldsymbol{R}_{dq} - \beta_{02}G_{\mathrm{CCF}}(\boldsymbol{e}_1)$, the error dynamics (31) can be rewritten as

$$\begin{cases} \dot{\boldsymbol{e}}_1 = \boldsymbol{e}_2 - \beta_{01}|\boldsymbol{e}_1|^{\alpha_1}\mathrm{sgn}(\boldsymbol{e}_1) \\ \dot{\boldsymbol{e}}_2 = \boldsymbol{G}_{dq} - \beta_{02}|\boldsymbol{e}_1|^{\alpha_2}\mathrm{sgn}(\boldsymbol{e}_1). \end{cases} \tag{32}$$

Definition 1 (see [38]): Suppose a vector $x = [x_1, x_2, \ldots, x_n] \in \mathbb{R}^n$, a continuous function $f(x): \mathbb{R}^n \to \mathbb{R}$ has homogeneous degree k with regard to $(\rho^{r_1}x_1, \rho^{r_2}x_2, \ldots, \rho^{r_n}x_n)$ if $f(\rho^{r_1}x_1, \rho^{r_2}x_2, \ldots, \rho^{r_n}x_n) = \rho^k f(x)$, $\forall \rho > 0$, where $k > \min\{r_i\}$, $i = 1,2,\ldots,n$. A differential system $\dot{x} = f(x)$, with continuous function $f(x): \mathbb{R}^n \to \mathbb{R}^n$, has homogeneous degree k with regard to $(\rho^{r_1}x_1, \rho^{r_2}x_2, \ldots, \rho^{r_n}x_n)$ if $f(\rho^{r_1}x_1, \rho^{r_2}x_2, \ldots, \rho^{r_n}x_n) = \rho^{k+r_i}f(x), \forall \rho > 0$, where $k > \min\{r_i\}$, $i = 1,2,\ldots,n$.

Lemma 1 (see [39]): Consider the system $\dot{x} = f(x(t))$, $f(0) = 0$, $x \in U \subset \mathbb{R}^n$, where $f: U \to \mathbb{R}^n$ is a continuous function on an open neighborhood U of the origin $x = 0$. Assume the existence of the Lyapunov function $V(x): U_1 \to \mathbb{R}$, where $U_1 \subseteq U \subseteq \mathbb{R}^n$ is a neighborhood of the origin, and

$$\dot{V}(x,t) \le -cV^{\gamma}(x,t) \quad \forall (x) \in U_1 \backslash \{0\} \tag{33}$$

where $c > 0$, $0 < \gamma < 1$. Then, the origin of the system is locally finite-time stable and the convergence time satisfies $T \le V^{1-\gamma}(x(t_0), t_0)/c(1-\gamma)$ for any $x(t_0) \subset U_1$.

Theorem 1: Consider the dynamics of (32) and assume the lumped uncertainties and their first-order derivative are bounded, if the observer is designed as (30) and appropriate observer gains

β_{01} and β_{02}, the estimated errors $x(t) = [e_1(t), e_2(t)] \in \mathbb{R}^n$ will converge to the origin in a finite time.

Proof: To facilitate the analysis, taking d-axis as an example, the error dynamics in d-axis can be expressed as

$$\begin{cases} \dot{e}_{d1} = e_{d2} - \beta_{01}|e_{d1}|^{\alpha_1}\mathrm{sgn}(e_{d1}) \\ \dot{e}_{d2} = G_d - \beta_{02}|e_{d1}|^{\alpha_2}\mathrm{sgn}(e_{d1}). \end{cases} \tag{34}$$

Given (34), if the term G_d is omitted, then the auxiliary system can be expressed as

$$\begin{cases} \dot{e}_{d1} = e_{d2} - \beta_{01}|e_{d1}|^{\alpha_1}\mathrm{sgn}(e_{d1}) \\ \dot{e}_{d2} = -\beta_{02}|e_{d1}|^{\alpha_2}\mathrm{sgn}(e_{d1}). \end{cases} \tag{35}$$

According to Definition 1, (35) is homogeneous of degree $\alpha_1 - 1$ with respect to the weights $(1, \alpha_1)$.

Then, the scalar function $V_0(\alpha, e)$ is defined as

$$V_0(\alpha, e) = \varsigma^\top P \varsigma \tag{36}$$

where $\varsigma^\top = [e_{d1}^{\frac{1}{r_1}} e_{d2}^{\frac{1}{r_2}}]$, $r_i = (i-1)\alpha - (i-2), i = 1, 2$; Q is a symmetric positive definite matrix and the symmetric positive matrix P satisfies a Lyapunov equation [37]

$$A^\top P + PA = -Q. \tag{37}$$

Considering that A can be Hurwitz if β_{01} and β_{02} are reasonably set, so e_{d1} and e_{d2} are asymptotically stable.

Note that system (35) is a homogeneous vector field of degree $m = \alpha - 1 < 0$ with respect to weights $r_i = (i-1)\alpha - (i-2), i = 1, 2$ [41].

Considering $V_0(\alpha, \rho^{r_i} e) = \rho^{r_i} V_0(\alpha, e)$, V_0 is homogeneous of degree $2r_1 = 2$ with respect to the weights (r_1, r_2) [42]. Then, due to $\dot{V}_0|_{G_d=0} = \frac{\partial V_0}{\partial e}\frac{\partial e}{\partial t}$, the degree of $\dot{V}_0$ is defined as $\hbar_{\dot{V}_0} = \hbar_{V_1} + \hbar_\alpha = 2 + \alpha - 1$ with respect to the weights (r_1, r_2). Based on Rayleigh's inequalities, it yields

$$\dot{V}_0|_{G_d=0} \le -\frac{\lambda_{\min}(Q)}{\lambda_{\max}(P)^{\frac{\alpha+1}{2}}} V_0^{\frac{\alpha+1}{2}} = -c_1 V_0^{\varepsilon_1} \tag{38}$$

where $\lambda_{\min}(Q)$ and $\lambda_{\max}(P)$ represent the minimum and the maximum eigenvalue of Q and P, respectively; $c_1 = \lambda_{\min}(Q)/\lambda_{\max}(P)^{(\alpha+1)/2}$ and $\varepsilon_1 = (\alpha+1)/2$.

Then, when $G_d \neq 0$ is satisfied, one can get

$$\dot{V}_0|_{G_d\neq 0} = \frac{\partial V_0}{\partial e}\frac{\partial e}{\partial t}|_{G_d(t)=0} - \frac{\partial V_0}{\partial e_{d2}} G_d. \tag{39}$$

Note that $\frac{\partial V_0}{\partial e_{d2}}$ is homogeneous of degree $\hbar_{e_{d2}} = \hbar_{V_1} - r_2 = 2 - \alpha$ with respect to the weights (r_1, r_2). Moreover, assume there exists a positive constant Φ satisfying $|G_d| \le \Phi$. Then, the following inequality can be obtained

$$\begin{aligned} \left|\frac{\partial V_0}{\partial e_{d2}}\right| G_d &\le \left|\frac{\frac{\partial V_0}{\partial e_{d2}}}{V_0^{\frac{2-\alpha}{2}}}\right| V_0^{\frac{2-\alpha}{2}} \Phi \\ &= k(\alpha, e_{d2}) \Phi V_0^{\frac{2-\alpha}{2}} \\ &= c_2 V_0^{\varepsilon_2} \end{aligned} \tag{40}$$

where $c_2 = k(\alpha, e_{d2})\Phi$, $\varepsilon_2 = (2-\alpha)/2$.

By combining (38) and (40), the following inequation holds:

$$\dot{V}_0 \le -c_1 V_0^{\varepsilon_1} + c_2 V_0^{\varepsilon_2}. \tag{41}$$

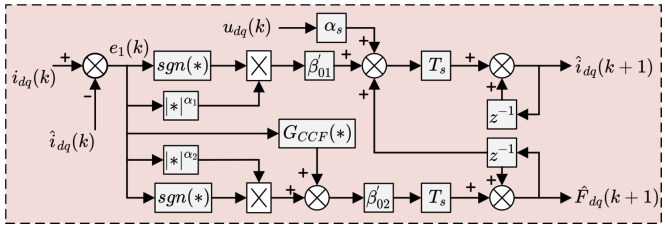

Fig. 3. Block diagram of the proposed NFTESO.

In view of (41), the following two cases are considered.

1) Case 1: When $V_0 \ge 1$, the following inequality can be obtained:

$$\dot{V}_0 \le -c_1 V_0^{\varepsilon_1} + c_2 V_0. \tag{42}$$

According to Lemma 1, V_0 will converge to $V_0 = 1$ within finite time t_{f1}, with $t_{f1} = \frac{\ln(1 - \frac{c_2}{c_1} V_0^{1-\varepsilon_1}(\varsigma(0)))}{c_2(\varepsilon_1 - 1)}$.

2) Case 2: When $V_0 < 1$, by selecting a parameter c_0 satisfying $0 < c_0 < 1 - c_2/c_1$, (41) can be rewritten as

$$\begin{aligned} \dot{V}_0 &\le -c_1 V_0^{\varepsilon_1} + c_2 V_0^{\varepsilon_2} \\ &= -c_1 c_0 V_0^{\varepsilon_1} - (c_1(1-c_0) V_0^{\varepsilon_1 - \varepsilon_2} - c_0) V_0^{\varepsilon_2}. \end{aligned} \tag{43}$$

Based on (43), we can obtain that $\dot{V}_0 \le 0$ when $V_0^{\varepsilon_1 - \varepsilon_2} > \frac{c_2}{c_1(1-c_0)}$ is satisfied. V_0 will converge to

$$V_0 \le \left(\frac{c_2}{c_1(1-c_0)}\right)^{\frac{1}{\varepsilon_1 - \varepsilon_2}}. \tag{44}$$

According to Lemma 1, the convergence time t_{f2} satisfies $t_{f2} \le \frac{V_0^{1-\varepsilon_1}(t_{f1})}{c_1 c_0 (1-\varepsilon_1)}$. Then, the Lyapunov function will converge to (44) within finite $t_f = t_{f1} + t_{f2}$. For the error dynamics described as (34), the estimated errors e_{d1} and e_{d2} will converge to bounded regions in a finite time. This completes the proof. Moreover, the stability analysis for the q-axis is similar to that for the d-axis, which is omitted here.

Furthermore, since the peaking phenomenon is usually caused by the high bandwidth of the observer, an observation error-based bandwidth tuning scheme is given as follows:

$$\begin{cases} \omega_0 = \omega_{\min}, & ||\boldsymbol{e}_1|| \ge \sigma \\ \omega_0 = \omega_{\max}, & ||\boldsymbol{e}_1|| < \sigma \end{cases} \tag{45}$$

where σ is the tunable parameter and $\omega_{\min}$ and $\omega_{\max}$ are the lower and upper limits of observer bandwidth gain, respectively.

Then, by combining (30) and (45), the proposed NFTESO is constructed as

$$\begin{cases} \boldsymbol{e}_1 = \boldsymbol{i}_{dq} - \hat{\boldsymbol{i}}_{dq} \\ \dot{\hat{\boldsymbol{i}}}_{dq} = \varepsilon_s \boldsymbol{u}_{dq} + \hat{\boldsymbol{F}}_{dq} + \beta'_{01}|\boldsymbol{e}_{dq}|^{\alpha_1}\mathrm{sgn}(\boldsymbol{e}_1) \\ \dot{\hat{\boldsymbol{F}}}_{dq} = \beta'_{02}\left(|\boldsymbol{e}_1|^{\alpha_2}\mathrm{sgn}(\boldsymbol{e}_1) + G_{\mathrm{CCF}}(\boldsymbol{e}_1)\right). \end{cases} \tag{46}$$

where $\beta'_{01} = 2\omega_0$ and $\beta'_{02} = \omega_0^2$, with ω_0 obtained by (45). The block diagram of the proposed NFTESO is shown in Fig. 3.

C. NFTESO-MFPCC

By combining (8) and (28), and using the Euler forward method, the proposed NFTESO for MFPCC can be discretized

as

$$\begin{cases} \boldsymbol{e}_1(k) = \boldsymbol{i}_{dq}(k) - \hat{\boldsymbol{i}}_{dq}(k) \\ \hat{\boldsymbol{i}}_{dq}(k+1) = \hat{\boldsymbol{i}}_{dq}(k) + T_s\varepsilon_s \boldsymbol{u}_{dq}(k-1) \\ \qquad\qquad + T_s\left(\hat{\boldsymbol{F}}_{dq}(k) + \beta'_{01}|\boldsymbol{e}_1(k)|^{\alpha_1}\mathrm{sgn}\left(\boldsymbol{e}_1(k)\right)\right) \\ \hat{\boldsymbol{F}}_{dq}(k+1) = \hat{\boldsymbol{F}}_{dq}(k) + T_s\left(\beta'_{02}|\boldsymbol{e}_1(k)|^{\alpha_2}\mathrm{sgn}\left(\boldsymbol{e}_1(k)\right)\right) \\ \qquad\qquad + T_s\beta'_{02}G_{\mathrm{CCF}}(\boldsymbol{e}_1(k)). \end{cases} \tag{47}$$

There, when the one-step compensation is implemented, the reference voltage vector of the proposed NFTESO-MFPCC can be derived as

$$\begin{cases} u_d^*(k) = \frac{i_d^* - \hat{i}_d(k+1)}{\varepsilon_s T_s} - \frac{\hat{F}_d(k+1)}{\varepsilon_s} \\ u_q^*(k) = \frac{i_q^* - \hat{i}_q(k+1)}{\varepsilon_s T_s} - \frac{\hat{F}_q(k+1)}{\varepsilon_s} \end{cases} \tag{48}$$

where $\hat{i}_d(k+1)$, $\hat{i}_q(k+1)$, $\hat{F}_d(k+1)$, and $\hat{F}_q(k+1)$ can be obtained from (47). Furthermore, considering that the sampling period T_s is short, it can be assumed that i_d^*, i_q^*, and ω_e^* remain unchanged in two adjacent sampling periods, e.g., $i_d^*(k+2) \approx i_d^*(k)$, $i_q^*(k+2) \approx i_q^*(k)$, and $\omega_e^*(k+2) \approx \omega_e^*(k)$.

Furthermore, the analysis of closed-loop stability of the control system is as follows.

By using the Taylor series method, the term $|\boldsymbol{e}_1(k)|^{\alpha_1}\mathrm{sgn}(\boldsymbol{e}_1(k))$ can be expanded. For convenience of analysis, assume that after a finite time, NFTESO has converged, so the observation error $\boldsymbol{e}_1(k)$ is small. Therefore, the higher order terms of the Taylor expansion can be ignored. Moreover, considering that the observation error of the CCF is bounded and the observation gains β'_{01} and β'_{02} can be adjusted to compensate for the approximation error, (47) can be approximately written as

$$\begin{cases} \boldsymbol{e}_1(k) = \boldsymbol{i}_{dq}(k) - \hat{\boldsymbol{i}}_{dq}(k) \\ \hat{\boldsymbol{i}}_{dq}(k+1) = \hat{\boldsymbol{i}}_{dq}(k) + T_s\varepsilon_s \boldsymbol{u}_{dq}(k-1) \\ \qquad\qquad + T_s\left(\hat{\boldsymbol{F}}_{dq}(k) + \beta''_{01}\boldsymbol{e}_1(k)\right) \\ \hat{\boldsymbol{F}}_{dq}(k+1) = \hat{\boldsymbol{F}}_{dq}(k) + (\beta''_{02}\boldsymbol{e}_1(k)) \end{cases} \tag{49}$$

where β''_{01} and β''_{02} denote the observation gains with compensation.

Then, to analyze the impact of parameter mismatch on closed-loop stability, (1) can be rewritten as

$$\begin{cases} \frac{di_d}{dt} = \frac{u_d}{L_s} + F_d \\ \frac{di_q}{dt} = \frac{u_q}{L_s} + F_q. \end{cases} \tag{50}$$

By combining (48), (49), and (50), and taking the q-axis as an example, the closed-loop transfer function in the discrete domain can be derived as follows:

$$\frac{i_q(z)}{i_q^*(z)} = \frac{da}{z(b+cd)} \tag{51}$$

where the coefficients a, b, c, and d can be expressed as

$$\begin{cases} a = (z-1)(z-1+\beta''_{01}T_s) + \beta''_{02}T_s^2 \\ b = L_s z(z-1)^2 + L_s(z-1)^2\beta''_{01}T_s \\ c = (z-1)\beta''_{01}T_s + z\beta''_{02}T_s^2 \\ d = 1/\varepsilon_s. \end{cases} \tag{52}$$

From (51) and (52), it is seen that once the estimation converges, the control loop can be represented as a seventh-order system containing seven poles and five zeros. When $\varepsilon_s = 1/L_s$, the five poles and zeros cancel each other out, leaving two poles located at the origin. The corresponding closed-loop transfer function is $i_q(z) = z^{-2}i_q^*(z)$, indicating that the control system realizes deadbeat response.

In addition, Fig. 4 illustrates the distribution of closed-loop poles of the motor under various operating conditions as the observer gains vary. It can be seen from Fig. 4(a) that all closed-loop poles are positioned on the positive real axis within the unit circle when the control gain is set to $au_s = 1/L_s$. In addition, poles are located at the origin for different bandwidths. This indicates that the control system is stable with zero oscillation frequency. Moreover, as the observer bandwidth increases, the poles approach the origin, leading to faster response times. Therefore, increasing the observer gains appropriately can enhance the dynamic response when the motor operates at nominal parameters. In addition, Fig. 4(b) shows the distribution of closed-loop poles as the observer gains change when the control gain becomes $\varepsilon_s = 0.5/L_s$. It can be seen that all closed-loop poles are located within the unit circle, so the control system remains stable. Moreover, as the observer gains increase, the closed-loop conjugate poles become closer to the origin, indicating an improvement in the system's dynamic response performance. However, the imaginary part of the closed-loop conjugate pole also increases with the increase of observer gains, which may lead to an increase in oscillation frequency and overshoot of the control system, making it more sensitive to noise and unmodeled dynamics. Therefore, a balance should be achieved between dynamic response and stability. Furthermore, as shown in Fig. 4(c), when the control gain is changed to $\varepsilon_s = 1.5/L_s$, the distribution of the closed-loop poles changes with the variation of the observer gains. It can be seen that all the poles are within the unit circle, indicating that the control system remains stable. However, as the observer gains increase, the imaginary part of the closed-loop conjugate poles increases more significantly, gradually approaching the stability boundary, which exacerbates the overshoot and oscillation of the control system.

In addition, the parameter tuning guidance for NFTESO is as follows: $\omega_{\min}$ and $\omega_{\max}$ should be selected to ensure that the matrix A is Hurwitz stable. In this article, $\omega_{\min} = 2000$, $\omega_{\max} = 2500$. Moreover, regarding the CCF, as analyzed in Section II, the resonant frequency ω_r is 6 times the motor angular velocity, i.e., $\omega_r = \pm 6\omega_e$, and the cutoff frequency coefficient η is 0.005. Moreover, to ensure the fairness of the comparison experiments, the values of control gain ε_s in all the comparison

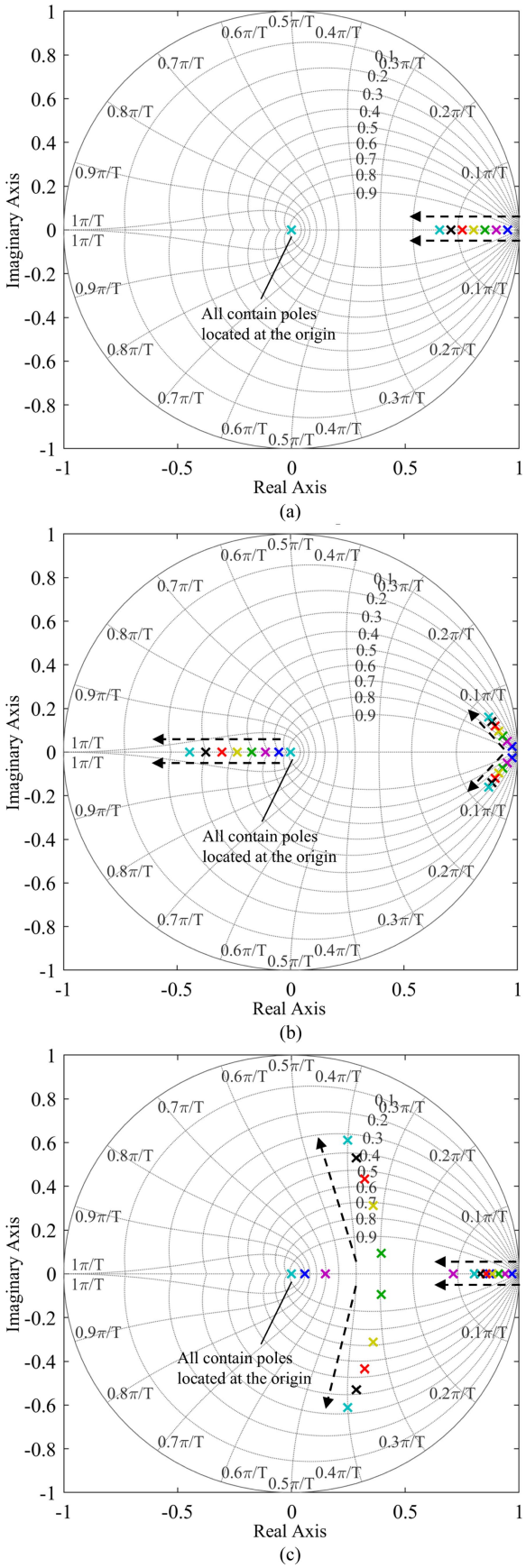

Fig. 4. Distribution of closed-loop poles and zeros under different conditions as the observer bandwidth varies from 1000 to 7000. (a) $\varepsilon_s = 1/L_s$. (b) $\varepsilon_s = 0.5/L_s$. (c) $\varepsilon_s = 1.5/L_s$.

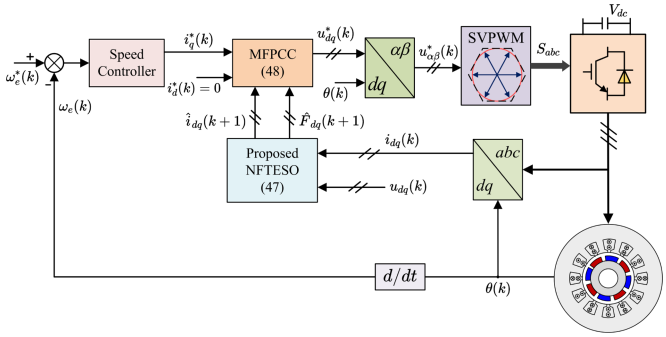

Fig. 5. Block diagram of the proposed control scheme.

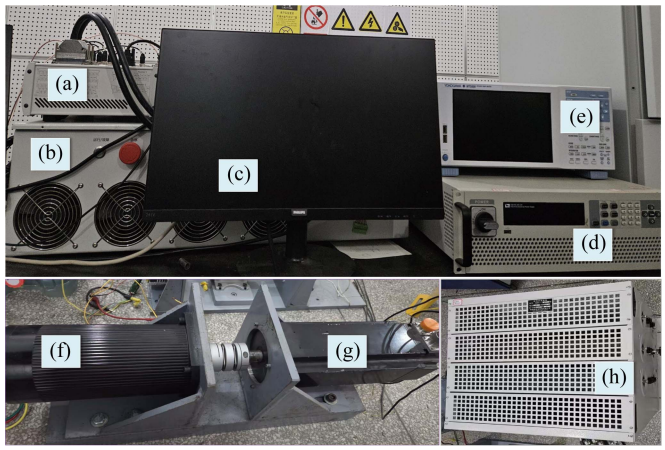

Fig. 6. Experimental platform. (a) dSPACE DS1202. (b) Power module. (c) Computer. (d) DC voltage source. (e) Power analyzer. (f) PMSM. (g) Load motor. (h) Resistance box.

algorithms are the same, i.e. $\varepsilon_s = 666.7$. The block diagram of the entire control scheme for PMSM drives is shown in Fig. 5.

Remark 1: The ultralocal model-based MFPCC strategy does not rely on PMSM parameters. Instead, it uses a highly simplified and universal input–output model to represent the dynamics of the system. In this strategy, the lumped uncertainty $\boldsymbol{F}_{dq}$ is key, covering changes in internal parameters (such as variations in inductance and resistance), external load disturbances, and all unmodeled dynamics. It only needs information on current and voltage and estimates the value of $\boldsymbol{F}_{dq}$ online. Therefore, it achieves immunity to parameter variations, demonstrating strong robustness.

Remark 2: In the proposed method, variations in inductance are automatically "absorbed" into the lumped uncertainty term $\boldsymbol{F}_{dq}$. The online estimation algorithm continuously updates $\boldsymbol{F}_{dq}$ in real time, incorporating the effects of inductance changes. In addition, the controller utilizes the updated $\boldsymbol{F}_{dq}$ to determine the voltage vector in each period, compensating for inductance perturbations naturally. As a result, MFPCC exhibits strong robustness to motor parameters. It is not only insensitive to inductance variations but also resilient to changes in resistance and magnetic flux linkage. However, the control gain ε_s is a constant that requires tuning. While it does not directly match the actual inductance, its value influences stability and dynamic

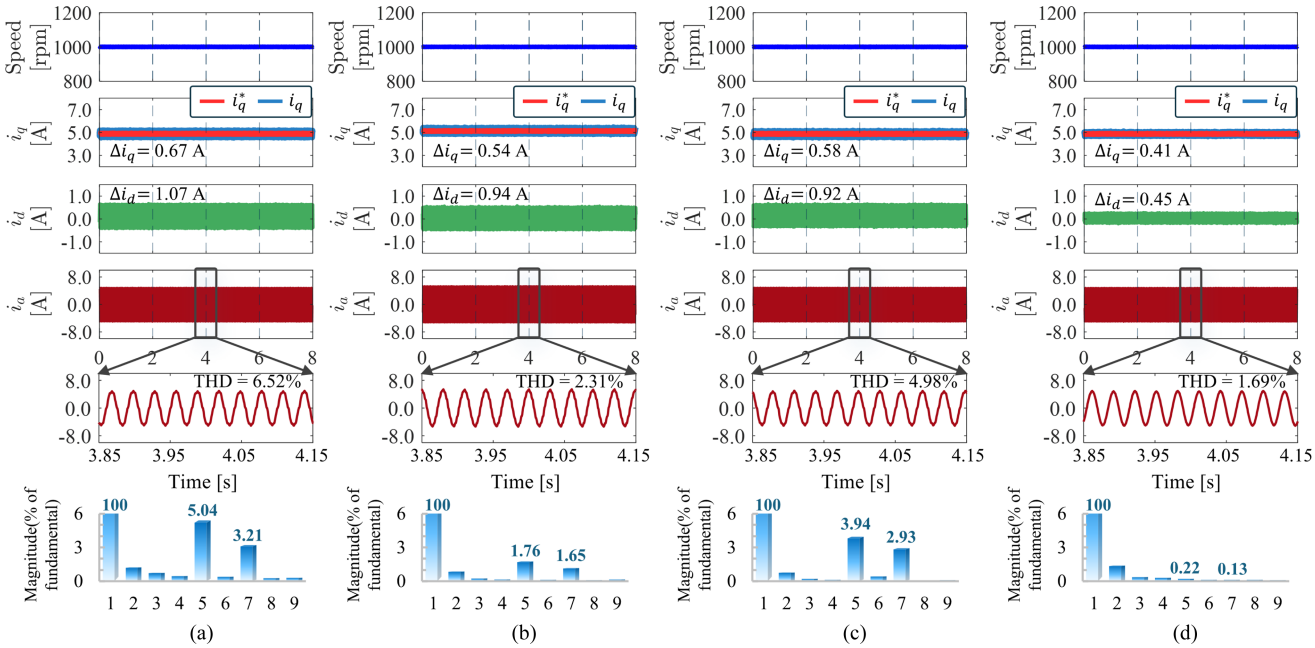

Fig. 7. Steady-state performance with nominal parameter ε_s under n_{ref} = 1000 r/min. (a) LESO-MFPCC. (b) GIESO-MFPCC. (c) FTESO-MFPCC. (d) NFTESO-MFPCC.

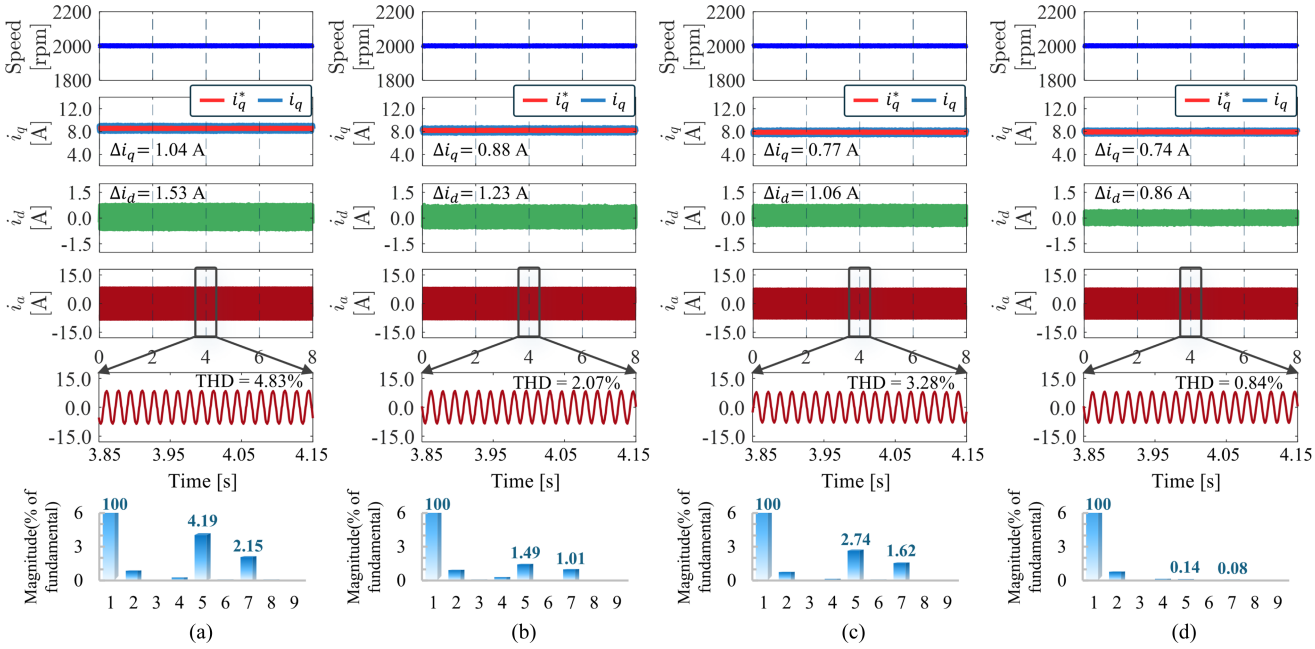

Fig. 8. Steady-state performance with nominal parameter ε_s under n_{ref} = 2000 r/min. (a) LESO-MFPCC. (b) GIESO-MFPCC. (c) FTESO-MFPCC. (d) NFTESO-MFPCC.

response. A rough initial value, such as the reciprocal of the nominal inductance, can be used, though performance can be improved through optimization tuning.

IV. Experimental Validation

The experimental platform is constructed as shown in Fig. 6. The load torque is provided by the load motor connected with the testing PMSM, and the parameters of the testing PMSM are shown in Table II. The dSPACE DS1202 real-time system is selected as the primary control system. The SVPWM with a 20 kHz switching frequency is utilized to generate the signals for the converter, which is composed of an Infineon SiC MOSFETmodule (model FF11MR12W1M1), and the dead time is 3.12 μs. Besides, the sampling frequencies of the speed and current loops are 2 and 20 kHz, respectively. Moreover, the

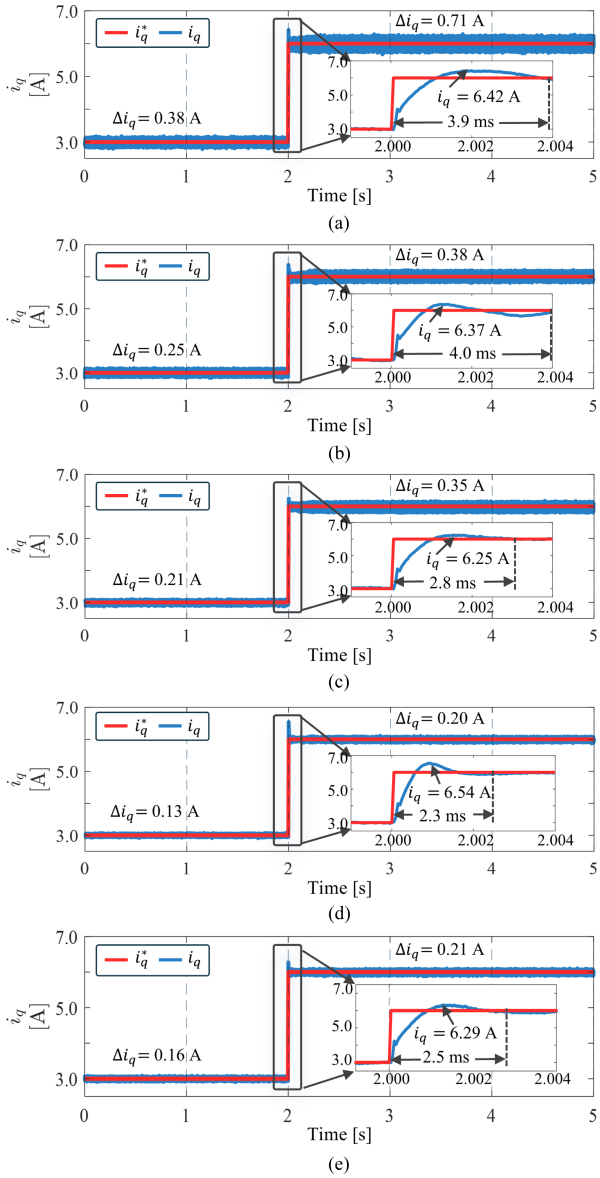

Fig. 9. i_q^* step response. (a) LESO-MFPCC. (b) GIESO-MFPCC. (c) FTESO-MFPCC. (d) NFTESO-MFPCC with fixed gain. (e) NFTESO-MFPCC.

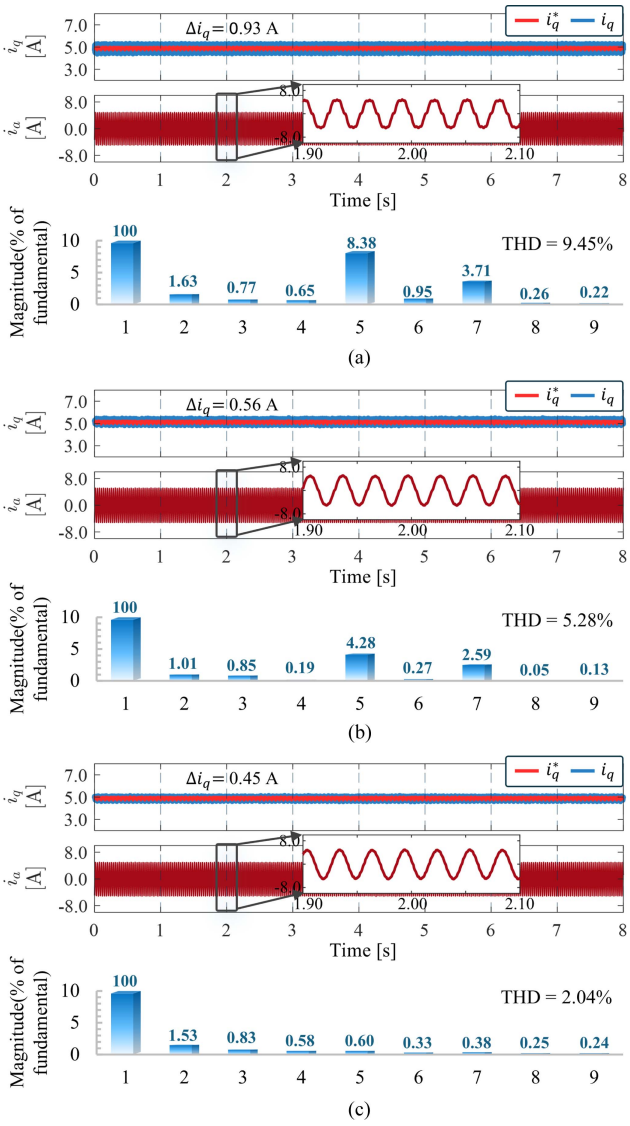

Fig. 10. Steady-state performance under $2\varepsilon_s$ with $n_{\text{ref}} = 1000$ r/min. (a) LESO-MFPCC. (b) AFKF-MFPCC. (c) NFTESO-MFPCC.

bandwidth of the NFTESO-MFPCC is 2.5 kHz, and the LESO-MFPCC, GIESO-MFPCC, and FTESO-MFPCC are selected as the comparative methods.

A. Steady-State Performance

Fig. 7 shows the steady-state performance of the comparative control methods with the nominal parameter ε_s at two different speeds, $n_{\text{ref}} = 1000$ r/min and $n_{\text{ref}} = 2000$ r/min. Regarding LESO-MFPCC, note that the q-axis and d -axis current fluctuations are 0.67 A and 1.07 A, respectively. The harmonic indices of the comparative control methods in the steady-state experiment are summarized in Table III. It can be seen that the fifth (5.40%) and seventh (3.21%) harmonics in i_a are the main components, consistent with the theoretical analysis, which proves that LESO-MFPCC is highly sensitive to periodic disturbances in PMSM drives. Moreover, the q-axis and d -axis current fluctuations of GIESO-MFPCC and FTESO-MFPCC are 0.54A and 0.94A, 0.58A and 0.92A, respectively. As a comparison, as shown in Fig. 7(d) and Table III, the current fluctuations of q-axis and d -axis of the proposed NFTESO-MFPCC are 0.41A and 0.45A, respectively. Furthermore, the fifth and seventh harmonics are 0.22% and 0.13%. Meanwhile,

TABLE II
PARAMETERS OF PMSM

Descriptions	Parameters	Nominal Values
Rated Power	P_n [kW]	1.6
Rated Speed	n [rpm]	2000
DC Voltage	U_{dc} [V]	150
Number of Pole Pairs	n_p	2
Resistance	R_s [Ω]	0.36
Inductance	L_s [mH]	1.5
Flux Linkage	ψ_f [Wb]	0.2

TABLE III
COMPARISON OF STEADY-STATE PERFORMANCE UNDER THE NOMINAL PARAMETER ε_s

	Methods	i_{a5th}	i_{a7th}	i_{aTHD}
n_{ref}=1000 rpm	LESO-MFPCC	5.40%	3.21%	6.52%
	GIESO-MFPCC	1.76%	1.65%	2.31%
	FTESO-MFPCC	3.94%	2.93%	4.98%
	NFTESO-MFPCC	0.22%	0.13%	1.69%
n_{ref}=2000 rpm	LESO-MFPCC	4.19%	2.15%	4.83%
	GIESO-MFPCC	1.49%	1.01%	2.07%
	FTESO-MFPCC	2.74%	1.62%	3.28%
	NFTESO-MFPCC	0.14%	0.08%	0.84%

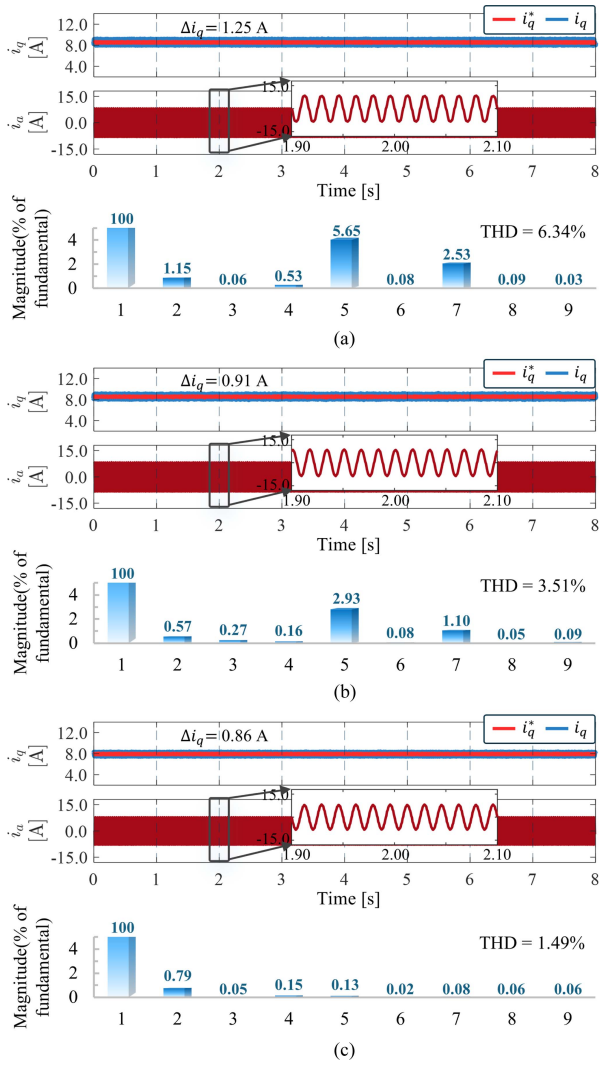

Fig. 11. Steady-state performance under $2\varepsilon_s$ with $n_{\text{ref}} = 2000$ r/min. (a) LESO-MFPCC. (b) AFKF-MFPCC. (c) NFTESO-MFPCC.

the THD index in the stator current of NFTESO-MFPCC is 1.69%, better than that of LESO-MFPCC (6.52%), GIESO-MFPCC (2.31%), and FTESO-MFPCC (4.98%). Hence, the steady-state performance with the nominal parameter shows that the proposed NFTESO-MFPCC control method achieves the best suppression performance of the periodic disturbance in

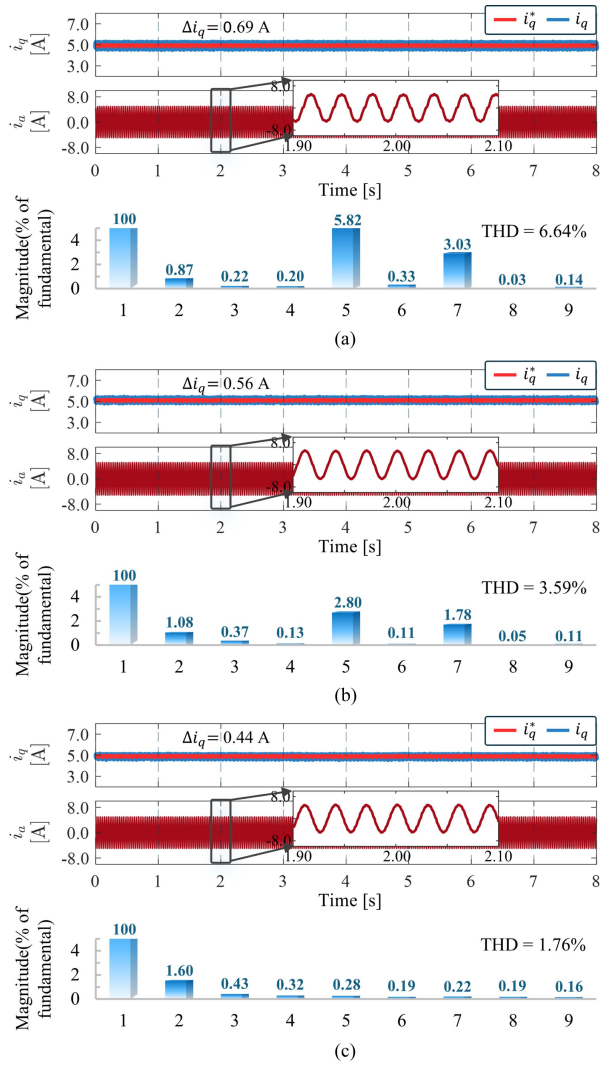

Fig. 12. Steady-state performance under $0.66\varepsilon_s$ with $n_{\text{ref}} = 1000$ r/min. (a) LESO-MFPCC. (b) AFKF-MFPCC. (c) NFTESO-MFPCC.

PMSM drives. Furthermore, as can be seen from Fig. 8, when the reference speed signal is changed to $n_{\text{ref}} = 2000$ r/min, the proposed method still achieves the smallest current fluctuations and the best THD indices.

B. Dynamic Performance

Fig. 9 demonstrates the results of the current dynamic response without a speed controller. In this test, the initial condition is set to $i_q^* = 3$A and suddenly changed to $i_q^* = 6$A at $t = 2$ s. Regarding the current fluctuation performance, for LESO-MFPCC, the current fluctuations of q-axis before and after the occurrence of the dynamic process are 0.38A and 0.71A, respectively. In addition, from the enlarged waveform in Fig. 9(a), the current tracking is achieved after 3.9 ms, with an overshoot of 0.42A. From Fig. 9(b), it is seen that with the same observer gains, the GIESO-MFPCC method has the longest settling time. Besides, due to the finite-time convergence characteristics and the nonlinear structure, the overshoot of FTESO is the smallest. In addition, to demonstrate the effect of the observer gain tuning

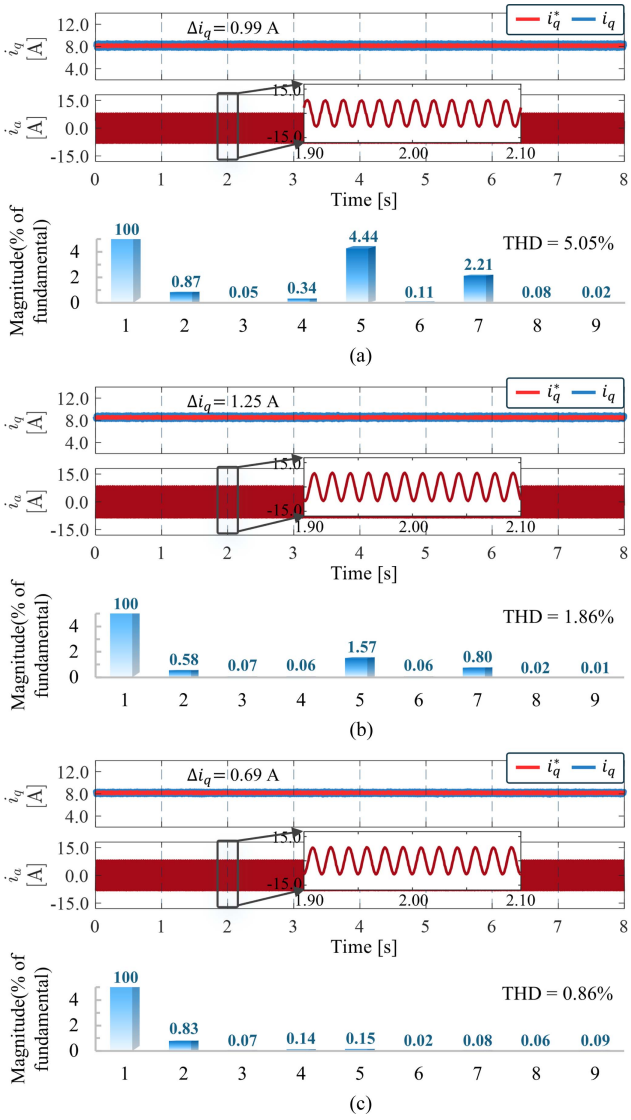

Fig. 13. Steady-state performance under $0.66\varepsilon_s$ with $n_{\text{ref}} = 2000$ r/min. (a) LESO-MFPCC. (b) AFKF-MFPCC. (c) NFTESO-MFPCC.

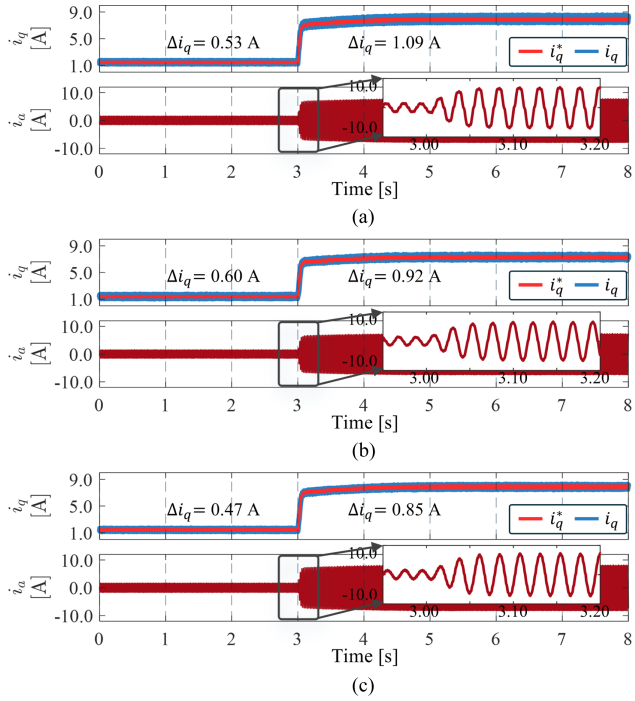

Fig. 14. Load step response under $2\varepsilon_s$ with $n_{\text{ref}} = 1500$ r/min. (a) LESO-MFPCC. (b) AFKF-MFPCC. (c) NFTESO-MFPCC.

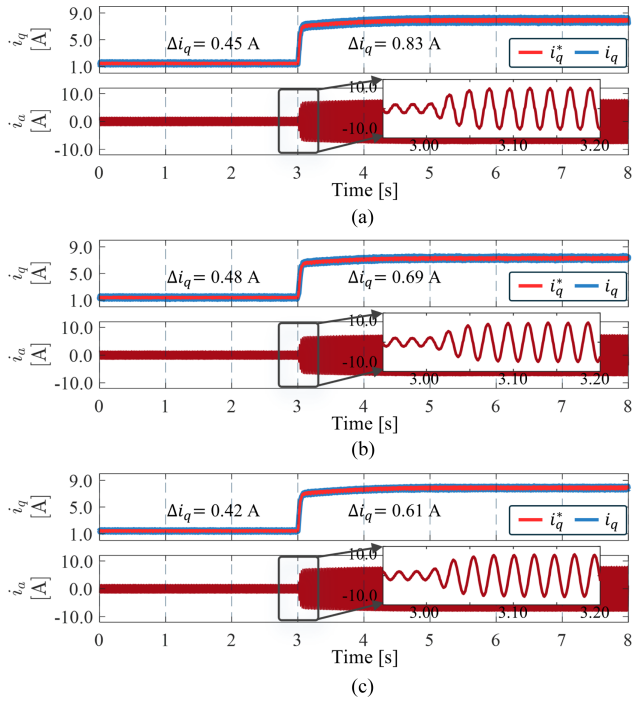

Fig. 15. Load step response under $0.66\varepsilon_s$ with $n_{\text{ref}} = 1500$ r/min. (a) LESO-MFPCC. (b) AFKF-MFPCC. (c) NFTESO-MFPCC.

strategy shown in (45), the NFTESO-MFPCC with a fixed-gain selected as $\omega_{\max}$ is added as a comparative strategy, and the experimental results are shown in Fig. 9(d). It can be seen that the introduction of the CCF term increases overshoot. Although the response time is only 2.3ms, i_q reaches 6.54 A.

Furthermore, as shown in Fig. 9(e), although the response time of the proposed method is 2.5 ms, the overshoot is 0.29 A. This indicates that due to the observer gain tuning strategy shown in (45), excellent overshoot control can be achieved. The essence of this strategy is to achieve a dynamic balance between dynamic response and noise suppression through estimation error feedback: when the estimation error is large, a smaller gain is selected to prioritize stability and avoid amplifying noise, which would further deteriorate performance; when the estimation error is small, a larger gain is chosen to maintain high observation accuracy and promptly suppress disturbances. In addition, due to the enhanced suppression capability for periodic disturbances, the proposed method achieves smaller and more stable q-axis current fluctuation values throughout the transient process, which are 0.16 and 0.21 A, respectively. Therefore, it is demonstrated that the proposed NFTESO-MFPCC exhibits a superior performance in the current dynamic response.

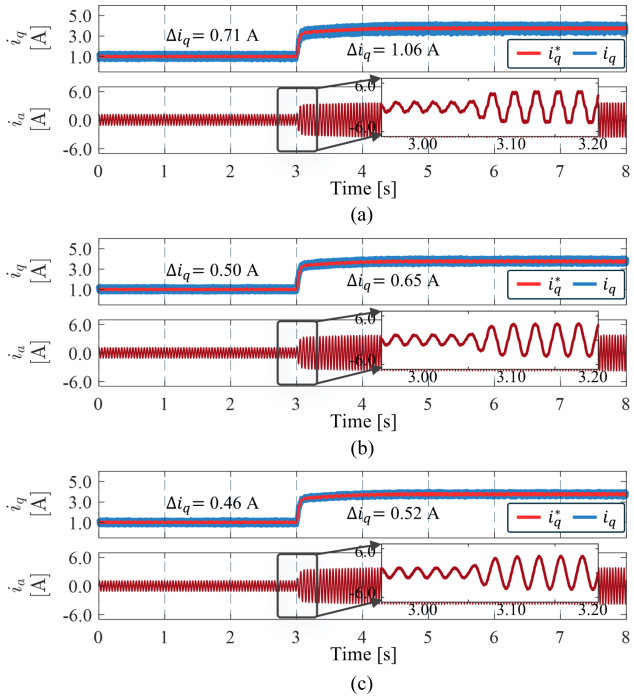

Fig. 16. Load step response under $2\varepsilon_s$ with $n_{\text{ref}} = 700$ r/min. (a) LESO-MFPCC. (b) AFKF-MFPCC. (c) NFTESO-MFPCC.

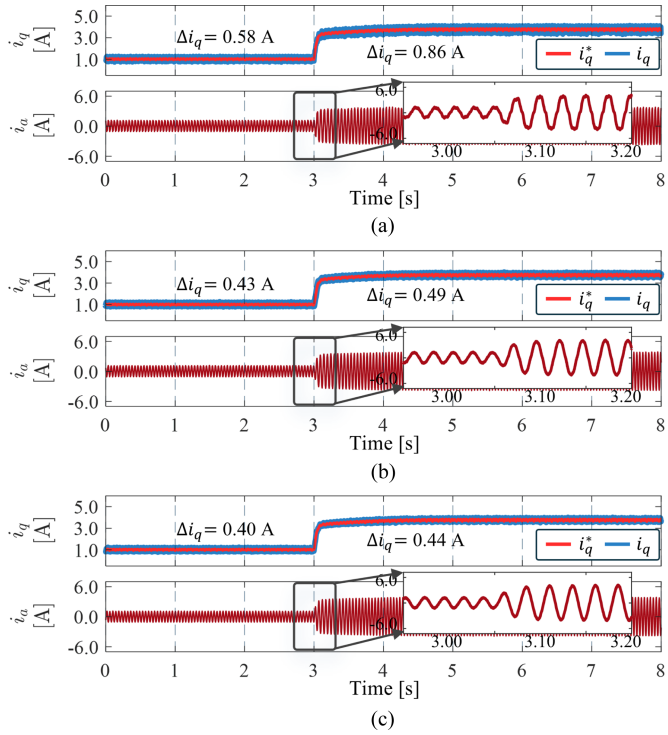

Fig. 17. Load step response under $0.66\varepsilon_s$ with $n_{\text{ref}} = 700$ r/min. (a) LESO-MFPCC. (b) AFKF-MFPCC. (c) NFTESO-MFPCC.

C. Robust to Parameter Mismatch

In this test, the comparative control methods are carried out under mismatched parameters. Since the control gain ε_s is closely related to the inductance, it is necessary to discuss the characteristics of the inductance variation. When the inductance parameters of PMSM are perturbed, they may either increase or decrease, mainly due to the following reasons.

1) When the current increases, the magnetic flux density in the motor core increases and gradually enters the saturation zone. In the saturation region, a large current increment is required to generate a small magnetic flux increment, resulting in a significant decrease in the equivalent inductance value. As the current increases, the inductance will decrease due to saturation.
2) At high temperatures, permanent magnets exhibit irreversible demagnetization, which corresponds to an increase in the d-axis magnetic reluctance, resulting in a reduction of the d-axis inductance. The magnitude of this temperature-induced change in L_d is generally smaller than the effect of saturation. In contrast, cooling the magnet improves magnetic properties, thereby causing a slight increase in L_d.
3) Other factors, such as production process deviations and aging, may cause the inductance variation, and the increase or decrease is uncertain.

From the above analysis, it can be seen that during the operation of PMSM, the magnetic saturation caused by the increase of current is the main reason for the inductance perturbation. The demagnetization of the permanent magnet caused by the temperature rise has the second-highest impact on the inductance perturbation after magnetic saturation. Since the nominal inductance value of the test PMSM is 1.5 mH ($\varepsilon_s = 666.7$), in this test, $\varepsilon_s = 1333$ and $\varepsilon_s = 444.4$ are designed to simulate operating conditions under parameter mismatch.

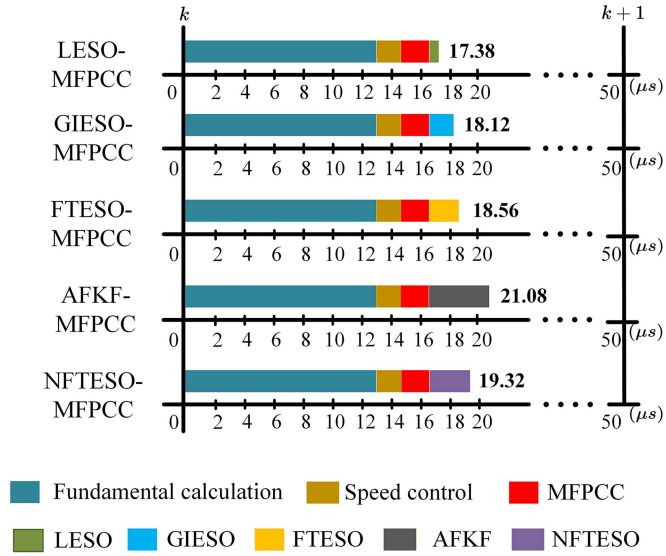

Fig. 18. Code execution time of each part of the comparative control methods.

To more clearly demonstrate the robustness to parameter mismatch of the proposed method, based on the augmented fading Kalman filter (AFKF) algorithm proposed in [43], AFKF-MFPCC is established and added along with LESO-MFPCC as comparative algorithms for parameter mismatch experiments. Fig. 10 shows the result of steady-state performance under

TABLE IV
COMPARISON OF STEADY-STATE PERFORMANCE WITH $2\varepsilon_s$

	Methods	i_{a5th}	i_{a7th}	i_{aTHD}
n_{ref}=1000 rpm	LESO-MFPCC	8.38%	3.71%	9.45%
	AFKF-MFPCC	4.28%	2.59%	5.28%
	NFTESO-MFPCC	0.60%	0.38%	2.04%
n_{ref}=2000 rpm	LESO-MFPCC	5.65%	2.53%	6.34%
	AFKF-MFPCC	2.93%	1.10%	3.51%
	NFTESO-MFPCC	0.13%	0.08%	1.49%

TABLE V
COMPARISON OF STEADY-STATE PERFORMANCE WITH $0.66\varepsilon_s$

	Methods	i_{a5th}	i_{a7th}	i_{aTHD}
n_{ref}=1000 rpm	LESO-MFPCC	5.82%	3.03%	6.64%
	AFKF-MFPCC	2.80%	1.78%	3.59%
	NFTESO-MFPCC	0.28%	0.22%	1.76%
n_{ref}=2000 rpm	LESO-MFPCC	4.44%	2.21%	5.05%
	AFKF-MFPCC	1.57%	0.80%	1.86%
	NFTESO-MFPCC	0.15%	0.08%	0.86%

mismatched parameter $2\varepsilon_s$ with the reference speed set to $n_{\text{ref}} = 1000$ r/min. It can be seen that compared to the results under nominal control gain, the current fluctuations of the two control schemes have degraded. For LESO-MFPCC, the values of those are 0.93A and 1.54A, respectively. Moreover, according to the Fourier analysis result, the fifth and seventh harmonics in i_a are 8.38% and 3.71%, respectively, with a THD index of 9.45%. For AFKF-MFPCC, the fifth and seventh harmonics in i_a are 4.28% and 2.59%, respectively, with a THD index of 5.28%. In contrast, as shown in Fig. 10(c), according to the Fourier analysis result, the fifth and seventh harmonics have been successfully eliminated by the proposed NFTESO. In addition, when the reference speed is set to $n_{\text{ref}} = 2000$ r/min, the comparative result is shown in Fig. 11. Note that the proposed NFTESO-MFPCC still achieves the best performance. Besides, the harmonic indices are summarized in Table IV. Furthermore, Figs. 12 and 13 show the results of steady-state performance with $0.66\varepsilon_s$ under $n_{\text{ref}} = 1000$ r/min and $n_{\text{ref}} = 2000$ r/min, respectively. The harmonic indices are shown in Table V. Thus, it can be concluded that the proposed NFTESO-MFPCC method achieves an excellent steady-state performance, even with mismatched control gains, exhibiting strong robustness against parameter perturbation.

In addition, a comparative experiment of the load step response with a mismatched parameter is conducted. In this test, the initial external load torque T_L is suddenly changed at $t = 3$ s. The results with the reference speed of $n_{\text{ref}} = 1500$ r/min and the mismatched parameter $2\varepsilon_s$ and $0.66\varepsilon_s$ are shown in Figs. 14 and 15, respectively. Note that compared to LESO-MFPCC and AFKF-MFPCC, the proposed NFTESO-MFPCC achieves the smallest fluctuations of the q-axis current before and after the transient process in two types of parameter mismatch conditions. Moreover, a similar experiment of the load step response with the mismatched parameters was carried out under the condition of $n_{\text{ref}} = 700$ r/min, with the results shown in Figs. 16 and 17. Again, it is observed that the proposed NFTESO-MFPCC still achieves the smallest fluctuations of the q-axis current throughout the transient process. Therefore, it can be concluded that under different parameter mismatch scenarios, the proposed control strategy achieves the best suppression of current fluctuations in both high-speed and low-speed operating conditions.

Remark 3: To fully verify the superiority and repeatability of the proposed method, a series of rigorous comparative experiments have been carried out, covering the following scenarios.

1) *Steady-state performance*: Including steady-state operation at medium and low speeds as well as high speeds.
2) *Dynamic response*: The q-axis current step response without a speed loop.
3) *Parameter sensitivity testing*: The performance was examined under two different parameter mismatches, including steady state at medium and low speeds, as well as sudden load changes at medium and low speeds.

Compared with the comparative methods, the proposed algorithm is the only one that maintains the best performance in all test cases. This consistent superior performance across various complex scenarios indisputably proves its high repeatability and engineering practical value.

D. Comparison of Computation Burden

The code computation time of each part of the comparative control methods is shown in Fig. 18. It can be seen that the computation time of the proposed method is 19.32 μs, which is the second longest among all comparison algorithms. However, it is less than half of the sampling period in the experiment. Therefore, the improvement in performance does not impose a significant burden on the digital implementation.

V. CONCLUSION

In this article, an enhanced MFPCC based on a novel NFTESO is proposed to mitigate aperiodic and periodic disturbances in the current loop while retaining the benefits of MFPCC. The proposed method significantly improves the ability to suppress aperiodic disturbances and effectively attenuates time-varying periodic harmonics simultaneously. In addition, utilizing Lyapunov theory, the theoretical analysis of finite-time stability for the proposed NFTESO is conducted. Moreover, the closed-loop stability of the proposed NFTESO-MFPCC control scheme is analyzed, and the influence of the inductance perturbation is discussed. The experimental results demonstrate that, compared to the existing control schemes, the proposed NFTESO-MFPCC not only reduces current fluctuations and harmonics but also ensures an excellent dynamic response and strong robustness, even under conditions of parameter perturbation. In the future, the authors will concentrate on further improving the proposed NFTESO-MFPCC and discussing the applications in more electrical driving scenarios.

REFERENCES

[1] S. Gao, Y. Wei, D. Zhang, H. Qi, Y. Wei, and Z. Yang, "Model-free hybrid parallel predictive speed control based on ultralocal model of PMSM for electric vehicles," *IEEE Trans. Ind. Electron.*, vol. 69, no. 10, pp. 9739–9748, Oct. 2022.

[2] H. Gao, Z. Zhang, Y. Liu, W. Huang, and H. Xue, "Development and analysis of dual three-phase PMSM with phase-shifted hybrid winding for aircraft electric propulsion application," *IEEE Trans. Transp. Electrific.*, vol. 10, no. 3, pp. 6497–6508, Sep. 2024.

[3] S. Zhao, X. Huang, Y. Fang, and J. Zhang, "Compensation of DC-link voltage fluctuation for railway traction PMSM in multiple low-switching frequency synchronous space vector modulation modes," *IEEE Trans. Veh. Technol.*, vol. 67, no. 1, pp. 235–250, Jan. 2018.

[4] Y. Du, T. Tao, W. Zhao, J. Ji, and Z. Li, "Quasi-fault-tolerant control for open-end winding five-phase PMSM with high-resistance connection failure using time-variant transform techniques," *IEEE Trans. Transp. Electrific.*, vol. 10, no. 4, pp. 7971–7983, Dec. 2024.

[5] P. Mani, R. Rajan, L. Shanmugam, and Y. H. Joo, "Adaptive fractional fuzzy integral sliding mode control for PMSM model," *IEEE Trans. Fuzzy Syst.*, vol. 27, no. 8, pp. 1674–1686, Aug. 2019.

[6] G. Bi, G. Zhang, G. Wang, Q. Wang, Y. Hu, and D. Xu, "Adaptive iterative learning control-based rotor position harmonic error suppression method for sensorless PMSM drives," *IEEE Trans. Ind. Electron.*, vol. 69, no. 11, pp. 10870–10881, Nov. 2022.

[7] B. Wang, M. Tian, Y. Yu, Q. Dong, and D. Xu, "Enhanced ADRC with quasi-resonant control for PMSM speed regulation considering aperiodic and periodic disturbances," *IEEE Trans. Transp. Electrific.*, vol. 8, no. 3, pp. 3568–3577, Sep. 2022.

[8] X. Sun, J. Cao, G. Lei, Y. Guo, and J. Zhu, "A composite sliding mode control for SPMSM drives based on a new hybrid reaching law with disturbance compensation," *IEEE Trans. Transp. Electrific.*, vol. 7, no. 3, pp. 1427–1436, Sep. 2021.

[9] M. Yang et al., "Enhanced model-free predictive speed control without weighting factors for PMSM based on newly designed cost function," *IEEE Trans. Transp. Electrific.*, vol. 10, no. 3, pp. 5703–5714, Sep. 2024.

[10] X. Sun, X. Lin, D. Guo, G. Lei, and M. Yao, "Improved deadbeat predictive current control with extended state observer for dual three-phase PMSMs," *IEEE Trans. Power Electron.*, vol. 39, no. 6, pp. 6769–6782, Jun. 2024.

[11] X. Zhang, Z. Wang, Z. Zhao, and M. Cheng, "Model predictive voltage control for SPMSM drives with parameter robustness optimization," *IEEE Trans. Transp. Electrific.*, vol. 8, no. 3, pp. 3151–3163, Sep. 2022.

[12] X. Li, W. Tian, X. Gao, Q. Yang, and R. Kennel, "A generalized observer-based robust predictive current control strategy for PMSM drive system," *IEEE Trans. Ind. Electron.*, vol. 69, no. 2, pp. 1322–1332, Feb. 2022.

[13] Q. Wang, G. Wang, N. Zhao, G. Zhang, Q. Cui, and D. Xu, "An impedance model-based multiparameter identification method of PMSM for both offline and online conditions," *IEEE Trans. Power Electron.*, vol. 36, no. 1, pp. 727–738, Jan. 2021.

[14] X. Yuan, Y. Zuo, Y. Fan, and C. H. T. Lee, "Model-free predictive current control of SPMSM drives using extended state observer," *IEEE Trans. Ind. Electron.*, vol. 69 no. 7, pp. 6540–6550, Jul. 2022.

[15] X. Zhang, C. Zhang, Z. Wang, and J. Rodríguez, "Motor-parameter-free model predictive current control for PMSM drives," *IEEE Trans. Ind. Electron.*, vol. 71 no. 6, pp. 5443–5452, Jun. 2024.

[16] Y. Zhang, J. Jin, and L. Huang, "Model-free predictive current control of PMSM drives based on extended state observer using ultralocal model," *IEEE Trans. Ind. Electron.*, vol. 68, no. 2, pp. 993–1003, Feb. 2021.

[17] H. Cao et al., "Improved ADRC with a cascade extended state observer based on quasi-generalized integrator for PMSM current disturbances attenuation," *IEEE Trans. Transp. Electrific.*, vol. 10, no. 1, pp. 2145–2157, Mar. 2024.

[18] Q. Hou et al., "Super-twisting extended state observer-based quasi-proportional-resonant controller for permanent magnet synchronous motor drive system," *IEEE Trans. Transp. Electrific.*, vol. 10, no. 1, pp. 1596–1604, Mar. 2024.

[19] Y. Bai et al., "High-gain nonlinear active disturbance rejection control strategy for traction permanent magnet motor drives," *IEEE Trans. Power Electron.*, vol. 37, no. 11, pp. 13135–13146, Nov. 2022.

[20] X. Li, S. Zhang, C. Zhang, Y. Zhou, and C. Zhang, "An improved deadbeat predictive current control scheme for open-winding permanent magnet synchronous motors drives with disturbance observer," *IEEE Trans. Power Electron.*, vol. 36, no. 4, pp. 4622–4632, Apr. 2021.

[21] X. Wu, J. Jin, and L. Huang, "Model-free predictive current control of SPMSM drives based on enhanced extended state observer," *IEEE Trans. Ind. Electron.*, vol. 71, no. 4, pp. 3461–3471, Apr. 2024.

[22] B. Guo, S. Bacha, M. Alamir, A. Hably, and C. Boudinet, "Generalized integrator-extended state observer with applications to grid-connected converters in the presence of disturbances," *IEEE Trans. Control Syst. Technol.*, vol. 29, no. 2, pp. 744–755, Mar. 2021.

[23] Y. Zuo et al., "Active disturbance rejection controller for smooth speed control of electric drives using adaptive generalized integrator extended state observer," *IEEE Trans. Power Electron.*, vol. 38, no. 4, pp. 4323–4334, Apr. 2023.

[24] X. Yang, H. Hu, H. Hu, Y. Liu, and Z. He, "A quasi-resonant extended state observer-based predictive current control strategy for three-phase PWM rectifier," *IEEE Trans. Ind. Electron.*, vol. 68, no. 12, pp. 13910–13917, Dec. 2022.

[25] Y. Zuo et al., "Sensorless control of IPMSM drives based on extended state observer with enhanced position estimation accuracy," *IEEE Trans. Power Electron.*, vol. 40, no. 1, pp. 787–800, Jan. 2025.

[26] S. Jia, D. Yang, P. Sun, D. Liang, and J. Si, "Decoupled current control using adaptive quasi resonant-based ESO for novel matrix-torque-component machines," *IEEE Trans. Power Electron.*, vol. 40, no. 6, pp. 8503–8515, Jun. 2025.

[27] F. Yang et al., "Complex coefficient active disturbance rejection controller for current harmonics suppression of IPMSM drives," *IEEE Trans. Power Electron.*, vol. 37, no. 9, pp. 10443–10454, Sep. 2022.

[28] S. Yin and X. Wang, "Composite disturbance suppression strategy for current loop of HSPMSG based on high frequency disturbance observer," *IEEE Trans. Transp. Electrific.*, vol. 10, no. 3, pp. 5762–2772, Sep. 2024.

[29] C. Luo, Z. Xu, K. Yang, W. Li, and Y. Huang, "Multiple disturbance suppression of IPMSM drives based on embedded discrete-time repetitive ADRC with optimized parameter selection," *IEEE Trans. Power Electron.*, vol. 39, no. 5, pp. 6052–6062, May 2024.

[30] H. Ding, Z. Zhu, X. Guo, S. Li, Z. Zhang, and K. Ma, "Improved ADRC with a disturbance-separation CESO based on complex coefficient-filter for current source rectifier," *IEEE Trans. Ind. Electron.*, vol. 73, no. 1, pp. 60–71, Jan. 2026.

[31] Z. Song and F. Zhou, "Observer-based predictive vector-resonant current control of permanent magnet synchronous machines," *IEEE Trans. Power Electron.*, vol. 34, no. 6, pp. 5969–5980, Jun. 2019.

[32] M. Tian, B. Wang, Y. Yu, Q. Dong, and D. Xu, "Static-errorless deadbeat predictive current control for PMSM current harmonics suppression based on vector resonant controller," *IEEE Trans. Power Electron.*, vol. 38, no. 4, pp. 4585–4595, Apr. 2023.

[33] M. Fliess and C. Join, "Model-free control," *Int. J. Control*, vol. 86, pp. 2228–2252, 2013.

[34] X. Yang, H. Hu, H. Hu, Y. Liu, and Z. He, "A quasi-resonant extended state observer-based predictive current control strategy for three phase PWM rectifier," *IEEE Trans. Ind. Electron.*, vol. 69, no. 12, pp. 13910–13917, Dec. 2022.

[35] C. Liu and J. Shang, "Sensorless drive strategy of open-end winding PMSM with zero-sequence current suppression," *IEEE Trans. Energy Convers.*, vol. 36, no. 4, pp. 2987–2997, Dec. 2021.

[36] Y. Li, Y. Hu, and W. Wu, "Complex-coefficient adaptive extended state observer for position estimation of PMSMs with enhanced robustness to disturbances," *IEEE J. Emerg. Sel. Topics Power Electron.*, vol. 13, no. 3, pp. 3324–3337, Jun. 2025.

[37] M. Basin, P. Yu, and Y. Shtessel, "Finite- and fixed-time differentiators utilising HOSM techniques," *IET Control Theory Appl.*, vol. 11, no. 8, pp. 1144–1152, 2017.

[38] J. Nie et al., "Finite-time output feedback path following control of underactuated MSV based on FTESO," *Ocean Eng.*, vol. 224, 2021, Art. no. 108660.

[39] S. Yu et al., "Continuous finite-time control for robotic manipulators with terminal sliding mode," *Automatica*, vol. 41, no. 11, pp. 1957–1964, 2005.

[40] L. Tao, J. Wang, D. Chen, and L. Zhou, "A robust hybrid complex coefficient filter without frequency coupling for position estimation accuracy improvement of PMSM," *IEEE J. Emerg. Sel. Topics Power Electron.*, vol. 12, no. 3, pp. 2799–2808, Jun. 2024.

[41] W. Perruquetti, T. Floquet, and E. Moulay, "Finite-time observers: Application to secure communication," *IEEE Trans. Autom. Control*, vol. 53, no. 1, pp. 356–360, Feb. 2008.

[42] H. Lu et al., "Finite-time extended state observer enhanced nonsingular terminal sliding mode control for buck converters in the presence of disturbances: Design, analysis and experiments," *Nonlinear Dyn.*, vol. 112, no. 9, pp. 7113–7127, 2024.

[43] F. Gao, Z. Yin, L. Li, T. Li, and J. Liu, "Gaussian noise suppression in deadbeat predictive current control of permanent magnet synchronous motors based on augmented fading Kalman filter," *IEEE Trans. Energy Convers.*, vol. 38, no. 2, pp. 1410–1420, Jun. 2023.

Changliang Dang was born in Shaanxi, China. He received the B.S. degree in electrical engineering from Southeast University, Nanjing, China, in 2006. He is currently working toward the Ph.D. degree in electrical engineering with Northwestern Polytechnical University, Xi'an, China.

From 2006 to 2008, he was with Toshiba Transformer Company, Ltd., Changzhou, China. From 2011 to 2018, he was with the Baoji University of Arts and Sciences, Baoji, China. His research interests include advanced control of power electronics and drives.

Yuanlin Wang (Member, IEEE) was born in Shaanxi, China, in 1988. He received the B.S. and M.S. degrees in electrical engineering from Northwestern Polytechnical University (NPU), Xi'an, China, in 2011 and 2014, respectively, and the Ph.D. degree in electrical engineering from Universitaet der Bundeswehr Muenchen, Neubiberg, Germany, in 2017.

He is currently an Associate Professor with NPU. His research interests include control and design for PMSM.

Jinli Lei was born in Shaanxi, China. She received the B.S. and M.S. degrees in automation from the Xi'an University of Science and Technology, Xi'an, China, in 2002 and 2005, respectively, and the Ph.D. degree in electrical engineering from Northwestern Polytechnical University, Xi'an, China, in 2014.

Her main research interests include advanced control of BLDCM drive systems.

Wenjuan Zhang was born in Shaanxi, China. She received the Ph.D. degree in power electronics and electric drives from the Xi'an University of Technology, Xi'an, China, in 2011.

In 2013, she was an Associate Professor with the Baoji University of Arts and Sciences, Baoji, China, where she was promoted to Professor in 2018. She is currently the Vice Dean of the Graduate School, Baoji University of Arts and Sciences, Baoji, China. Her research interests include wind power generation and its control, power electronics, and intelligent sensors.